Geochimica et Cosmochimica Acta 343 (2023) 64–83

Contents lists available at ScienceDirect

Geochimica et Cosmochimica Acta

journal homepage: www.elsevier.com/locate/gca

Exploring soluble and colloidally transported trace elements in stalagmites: The strontium-yttrium connection

J.T. Sliwinski [a,b,*], O. Kost [a], L. Endres [a], M. Iglesias [c], N. Haghipour [a], S. González-Lemos [d], H.M. Stoll [a]

[a] Geological Institute, ETH Zürich, Sonneggstrasse 5, 8092 Zürich, Switzerland
[b] School of Earth and Environmental Sciences, University of St. Andrews, Queen's Terrace, St. Andrews KY16 9TS, UK
[c] Departamento de Geología, C. Jesús Arias de Velasco, s/n, 33005 Oviedo, Asturias, Spain
[d] ASCIEM Consulting SLP, C/ Gutiérrez Herrero 52, 33402 Avilés, Spain

ARTICLE INFO

Article history:
Received 7 June 2022
Accepted 17 December 2022
Available online 21 December 2022
Associate editor: Adrian Immenhauser

Keywords:
Speleothem
Stalagmite
LA-ICP-MS
Confocal laser scanning microscopy
Trace elements
Paleoclimate
Glacial termination

ABSTRACT

While seasonality in speleothem trace element signatures is well-documented, the parameters that control the emergence of laminations vary between elements and tend to be multi-factorial. Here, we examine a series of active and fossil stalagmites from Asturias, Spain, with a particular focus on strontium and yttrium co-variations and fluorescent laminations. Coupled confocal fluorescence scanning light microscopy (layer counting) and time scales derived from accelerated mass spectrometry ($F^{14}C$) in active stalagmites confirm that fluorescent banding is annual. This banding is coincident with Y peaks and Sr troughs, which are among the most robust trace element markers of seasonality. Strontium concentrations (in particular, the strontium partition coefficient, D_{Sr}) are positively correlated with stalagmite growth rate and are likely controlled by solution supersaturation, which is in turn controlled by seasonal variations in cave ventilation. D_{Sr} can be estimated after correcting for prior calcite precipitation using coeval Mg/Ca ratios, and is consistent with both empirical and experimental values. Meanwhile, yttrium is a proxy for colloidal organic input, and its concentration in stalagmites is likely controlled by a combination of Y drip water flux, surface retention time (i.e., how long a drip and its associated organic matter are in contact with the stalagmite surface), and dilation within the matrix (hereafter referred to as "dilation"). Persistent Sr-Y anti-correlation can be explained as an interplay between the individual controls on each element, and a breakdown in this relationship may be indicative of past changes in cave ventilation and/or drip hydrology.

1. Introduction

Speleothems constitute a terrestrial paleoclimate archive with a wealth of chemical and isotopic information that is often "encrypted" by a multitude of complicating factors, the understanding of which is essential for robust interpretations. Trace element incorporation into stalagmites is accomplished in one of three general ways, as outlined by Fairchild and Treble (2009): (1) soluble trace elements are partitioned into the calcite lattice in the classical sense, wherein compatible and incompatible elements can be defined based on their ionic radii and their similarity to the prevalent cation (e.g., Mg^{2+} and Sr^{2+} substitute for Ca^{2+}); (2) poorly-soluble trace elements can be transported through the karst with the aid of various ligating/chelating agents, where colloidal organic matter (hereafter referred to as natural organic matter, or NOM) is most often invoked (Borsato et al., 2007; Hartland et al., 2012; Pearson et al., 2020). This class includes elements such as Y, Zn, Cu, Co, P and Pb, but it is unclear if the NOM is incorporated directly into the lattice with its trace element load, or if trace elements are first disassociated from NOM prior to incorporation. The elemental lability (i.e., its potential to dissociate from his host) must be considered here (Hartland et al., 2014), wherein moderately labile elements benefit both from enhanced transport and are able to easily dissociate from NOM to incorporate into the calcite lattice. Finally, (3) some trace element variations arise from the wholesale incorporation of particulate matter such as clay, sand and dust particles. The third incorporation mechanism is perhaps more relevant to stalagmites that experience periodic flooding (Gonzalez-Lemos et al., 2015) or receive input from aeolian dust sources in more arid climates (Frumkin and Stein, 2004; e.g., Goede et al., 1998), as well as pollen and other particulate matter from the local environment. Because the stalagmites in this

* Corresponding author at: School of Earth and Environmental Sciences, University of St. Andrews, Queen's Terrace, St. Andrews KY16 9TS, UK.
E-mail address: jts21@st-andrews.ac.uk (J.T. Sliwinski).

https://doi.org/10.1016/j.gca.2022.12.023
0016-7037/

study are located in the upper galleries of a cave system that is topographically shielded from dust sources, neither flooding nor aeolian dust are likely to make a contribution to the trace element budget. While dust and pollen input from the local environment cannot be ruled out, we focus in this study on trace element incorporation via the mechanisms outlined in (1) and (2) above. It should be noted that the term "partitioning" is intentionally avoided here in favor of "incorporation" when dealing with poorly-soluble elements. Similarly, given the potential of trace elements to incorporate via lattice defect sites or in conjunction with other phases, the speleothem distribution coefficient (SK_x) terminology was introduced by (Frisia et al., 2012) to account for all potential methods of incorporation, including the classical thermodynamic partitioning.

Here, we examine a collection of active and fossil stalagmites from Asturias, northern Spain, which is bounded by the Cantabrian mountains to the south and the Bay of Biscay to the north. We observe persistent and strong anti-correlations between Sr and Y in many stalagmites, which are coincident with fluorescence patterns and tied to variations in organic matter incorporation. Among colloidally transported elements, Y is exceptional in that it is extremely insoluble and therefore entirely dependent on organic ligands for transport (i.e., not labile; Hartland et al., 2014), unlike P, Zn and Cu (Hartland and Zitoun, 2018; Stoll et al., 2012). Furthermore, there are few if any isobaric interferences or polyatomic interferences on mass 89 when analyzing calcite by ICP-MS (Jochum et al., 2012), meaning that the signal to noise ratio is maximized for Y. Meanwhile, the choice of Sr as a counterpart to Y is governed by its relatively high concentration in the karst system, low potential for isobaric interferences by ICP-MS, and, relative to Mg, its low response to sea spray input (i.e., Sr from bedrock dissolution $\gg$ Sr from sea water) and sectoral zoning (Paquette and Reeder, 1995; Sliwinski and Stoll, 2021; Tremaine and Froelich, 2013). We begin by testing the classical notion that Sr incorporation is positively driven by growth rate (e.g., Lorens, 1981), and use covariations of this element with Y to build on a conceptual model proposed by previous authors, wherein Sr and Y represent soluble elements and colloidally transported elements (respectively). Finally, using active cave monitoring data, we make assertions about the dominant driving force of both on seasonal and inter-annual time scales.

2. Regional geological and climate setting

The Carboniferous limestones of northern Spain are host to many cave systems, including Cueva La Vallina, from which this study's samples were collected (Fig. 1; Stoll et al., 2015). These comprise thick sequences of laminated grey-black bituminous limestones, including micrites, microsparites and dolomicrites (Gasparrinia et al., 2003; Menéndez et al., 2018). Where dolomitized, associated stylolites can be found together with sulfides, which may influence the trace element budget of percolating drip waters. The cave is located within 5 km of the present-day coast, with an entrance 70 m above sea level (Stoll et al., 2013) located within a mixed-use terrain comprising pasture, planted eucalyptus (<60 years old based on trunk diameter) and native deciduous forests. Karst thickness above La Vallina is typically <30 m (Table 1), and the cave is roughly divided into an upper and lower gallery, with the upper gallery providing the majority of stalagmite samples and drip water monitoring sites (Fig. S1). The lower gallery hosts a stream that periodically aids in ventilating the cave air, as well as a single sample in this study that is situated beneath a grove of eucalyptus trees. Here, root infiltration is visible on the cave roof, while the remainder of the cave is largely unaffected. Other sampling sites in this study are situated beneath pasture, oak trees and mixed underbrush (fern).

The regional climate in Asturias is temperate and wet, with approximately 1,200 mm of annual precipitation. Average monthly temperatures vary between 10 and 20 °C in winter/summer months, and average monthly precipitation varies between 110 and 50 mm, respectively (Fig. S2). Potential evapotranspiration (PET) varies between 30 and 100 mm in winter/summer months (Thornthwaite, 1948), but conditions are seldom dry enough in summertime to inhibit soil microbial activity (i.e., drip water monitoring sites remain active with slowed drip rates throughout the summer). Drip water monitoring data indicate no appreciable drop in $[Ca^{2+}]$ in winter months (along with no evidence from Mg/Ca for enhanced PCP in these months), suggesting that soil pCO_2 does not drop significantly in the winter. However, cave air pCO_2 does decrease significantly in the wintertime when atmospheric temperatures drop below a threshold and begin to ventilate the cave system. This is particularly true in the lower gallery, where ventilation is aided by the ephemeral stream.

3. Methods

3.1. Sample collection and preparation

Samples were, for the most part, naturally broken and collected from the cave floor. A notable exception was made for active drip sites with associated stalagmites, whereby the topmost centimeters of the stalagmites were sawn off. The uppermost micrometers of these stalagmite fragments were scraped off and analyzed by X-ray powder diffraction (XRD) in a previous study to confirm the presence of only calcite on the actively-growing surface (Sliwinski and Stoll, 2021).

Fragments sawn perpendicular to the growth axis and mounted in epoxy (Araldite DY 026 + Laromin C260) and cured overnight at 50 °C, after which they were ground and polished with SiC abrasive paper and diamond suspension (respectively) to a 1 μm finish. This preparation enabled imaging by confocal microscopy (see below) as well as trace element determinations by LA-ICP-MS. A combination of these two methods allowed for a first-order approximation of the growth rate by fluorescent layer counting and/or Sr-Y peak counting, which then guided the sampling resolution of drilled ^{14}C sample powders. These powders were analyzed for by AMS (see below) in order to locate the "bomb spike" and confirm the active nature of the stalagmites (Genty and Deflandre, 1998). The bomb spike base determination method of Markowska et al. (2019) was used, wherein the inflection point of the ^{14}C record (the first point above baseline) was assigned an age corresponding to a delay of up to 4 years after 1955 (Hua et al., 2017), or the year 1959. Non-active stalagmites collected in earlier years followed a similar sample preparation procedure, including mounting in epoxy and polishing prior to imaging/analysis. These were not, however, analyzed by AMS (Table 1).

3.2. Accelerated Mass Spectrometry (AMS)

Samples were drilled at variable resolution (0.5–2 mm) using a 0.9 mm drill bit to obtain 2 mg powder, which was transferred into LabCo 4.5 mL vials. These vials were then purged with He for 10 min and calcite powders were converted to CO_2 through the addition of 85% H_3PO_4. The resulting CO_2 was analyzed using a gas-accepting ion source installed on a Mini Carbon Dating System (MICADAS) at the Laboratory of Ion Beam Physics, ETH Zurich (Synal et al., 2007). The result was normalized against standard Oxalic Acid II (NIST SRM 4990C) and corrected with radiocarbon-blank CO_2 (IAEA C-1). Two additional standards (IAEA C2 and coral CSTD) were measured in each sequence run to test the accuracy of

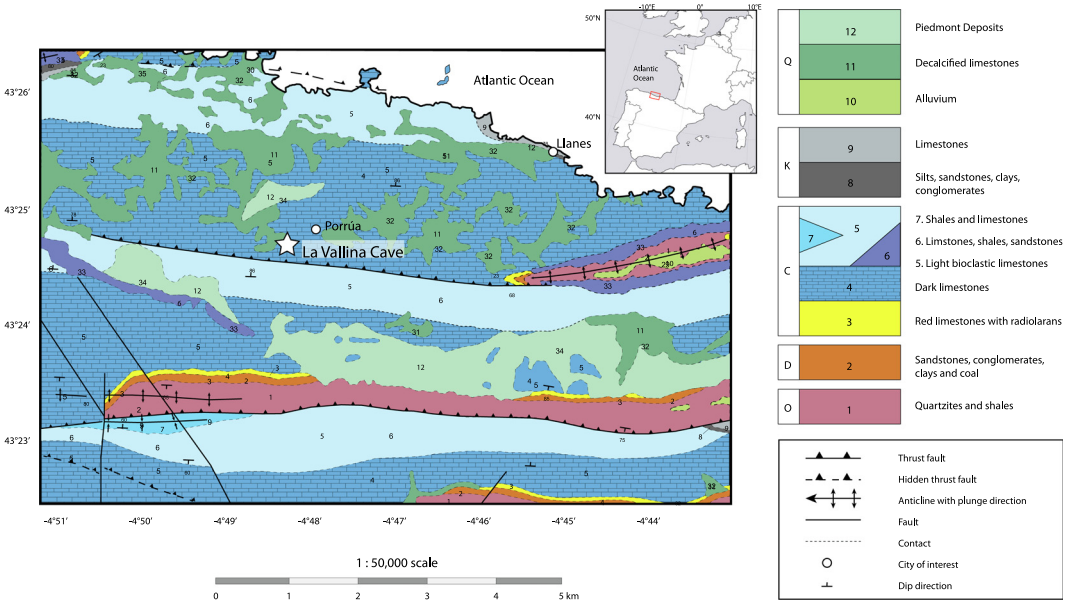

Fig. 1. Simplified geological map of the studied area in Asturias. Inset: Iberian peninsula, showing areal extent of the geological map in red square. Cave entrance denoted by starred location. Adapted after Martinez Garcia (1976), Instituto Geológico y Minero de España. O = Ordovician; D = Devonian; C = Carboniferous; K = Cretaceous; Q = Quaternary.

Table 1
Samples overview.

Sample	Gallery[a]	Monitor pts yr^{-1}	Min/Max pCO_2 [ppm]	Bedrock thickness	Drip rate range [mL min^{-1}] (avg)	Age span (ka)	Avg. growth rate (µm yr^{-1})[†]	Med. Sr/Ca[‡]	Med. Y/Ca[‡]
Active stalagmites									
MUS ("Mushroom")	L	4	500/3400	23	2.6–3.4 (3.0)	decades	148	0.036	0.000037
SKY ("Skyscraper")	U	12	510/4120	28	25 – 110 (92)	decades	131	0.034	0.037
PLA ("Playground")	U	4	550/4200	30	0.32–0.41 (0.37)	decades	66	0.077	0.0038
SNO ("Snowball")	U	4	660/1500	14	0.22–0.71 (0.47)	decades	320	0.055	0.00021
GUI ("Guillermina")	U/L	1	518/3180	8	0.04–0.03 (0.034)	decades	176	0.071	0.0027
Fossil stalagmites									
GAE ("Gael")	U					70–74*	55	0.12	0.00098
GAR ("Garth")	U					136–124**	25	0.063	0.00053
GEL ("Gelito")	U					~220–250	40	0.083	0.00090
GAL ("Galia")	U/L					5–8**	35	0.037	0.0012
GUL ("Gulda")	U					~8–13	18	0.034	0.00027

[†] Age span of intervals analyzed in this study in ka (fossil stalagmites) and decades for active stalagmites; does not include hiatuses.
[‡] mmol TE/mol Ca.
* Stoll et al., 2015; Stoll et al., 2022a,b.
** Stoll et al., 2013.
[a] U = upper; L = lower.

the measurements. Radiocarbon data were expressed as $F^{14}C$ (fraction of modern carbon) according to Reimer et al. (2004).

3.3. Confocal Laser Scanning Microscopy (CLSM)

Samples were imaged by CLSM (Olympus Fluoview 3000) at the Scientific Center for Optical and Electron Micrsocopy (ScopeM) at ETH Zurich using a wavelength of 488 nm (blue) and an emission detection window of 490–590 nm. A series of images taken at 100× magnification (~1.3 × 1.3 mm) were obtained with a ~10% overlap and automatically stitched to produce a fluorescence map of each region of interest. These images were imported into ImageJ/Fiji (Rasband, 2012) using the bioformats plugin to recognize the proprietary.oir file format. From here, point counting of individual layers and the distances between them was conducted using standard ImageJ tools and the length scale metadata stored in the individual files.

3.4. Laser ablation inductively-coupled plasma mass spectrometry (LA-ICP-MS)

Samples were analyzed inside of a Laurin Technic S155 2-vol ablation cell using an Australian Scientific Instruments (ASI) 193 nm Resolution ArF excimer laser under an atmosphere of high purity (5.0–6.0) He (370 mL/min) and N_2 (5.0 mL/min), which were mixed with Ar (~1.0 L/min) downstream of the ablation cell. Importantly, no signal smoothing device was used. Data were obtained with a square laser spot (20 µm width) ablating at 20 Hz and scanning across the sample surface at 20 µm/s. Laser scans were kept as parallel as possible to the growth axis, and as straight as possible to not ablate a track longer than the length of the sample. Data were collected on an Agilent 8800 Triple Quadrupole ICP-MS equipped with a collision/reaction cell (see Table S1 for more details), however, most analyses were performed without the reaction cell in order to optimize signal intensities. Raw LA-

ICP-MS data were reduced the TraceElements_IS.ipf data reduction scheme in Iolitev2.5 (Paton et al., 2010) on the IgorPro platform. Data were normalized to 39.5 wt% Ca, after which trace element concentrations were recalculated as ratios to Ca and reported in mmol mol^{-1}. Based on long-term reproducibility of the NIST610 synthetic glass standard, the precision of trace element analyses is better than 5% for elements well above the limit of detection, while accuracy is typically with 10% of the reference material concentration.

The spatial resolution of LA-ICP-MS transects is a complex function of laser spot size, scanning speed, laser ablation frequency, ICP-MS sampling time and sample washout time. These first four parameters varied in different samples between 20–30 μm, 20–30 μm s^{-1}, 20 Hz and 200–300 ms, respectively, while the washout time is typically ~0.7 s. This results in one data sample every 4–7 μm. The amplitude of trace element oscillations can be faithfully captured if the spot size is less than ~50% of the oscillation period, so a hypothetical 20 μm spot would capture a 40 μm oscillation with 5–10 data points. Laser transects were obtained as straight lines from well-polished surfaces, taking care to avoid voids and damaged areas where possible. Additional parallel transects were obtained to gain a qualitative assessment of the reproducibility of the method.

3.5. Growth rate estimates and trace element referencing

Growth rates were estimated in one of four ways, including two radiometric methods and two layer counting methods. Radiometric growth rate estimates were derived from published U-Th dates (Stoll et al., 2015; Stoll et al., 2013) in fossil stalagmites (GAE, GAR, GAL) or from $F^{14}C$ measurements in active stalagmites (GUI, MUS, SKY, PLA, SNO). In the latter case, the inflection point connecting baseline $F^{14}C$ to the bomb spike was set to 1959 following Markowska et al. (2019), and an average growth rate was calculated based on the position of this point and the tip (set to the collection date).

Annually-resolved growth rates were estimated in fossil and active stalagmites using layer counting methods specifically to derive relationships between growth rates and trace element variations. In the first method, fluorescent layers were marked on confocal images and referenced against an absolute length scale. These confocal images were imported into the GeoStar (laser ablation) software and georeferenced onto optical scans. Laser ablation data were in turn georeferenced onto the optical and confocal scans, allowing for comparison of growth rates (from confocal image) with trace element variations. However, because of uncertainty in the laser ablation stage reproducibility, and more importantly in the georeferencing of optical and confocal images, it is more reliable to compare *average* trace element concentrations and average growth rates (summing across several layers) than instantaneous growth rates (single-year) and their corresponding trace element concentrations. For two stalagmites (GAR and GEL), excellent fluorescent banding allowed for manual counting of ~3,000 layers (Stoll et al., 2022a), which were divided into sub-segments of 100 layers. The average growth rate across these sub-segments was correlated with average trace element ratios. Other stalagmites with shorter spans of countable fluorescent layers nevertheless showed excellent trace element cycles, and it was therefore possible to estimate instantaneous growth rates from LA-ICP-MS data.

A MATLAB script was written to allow for semi-automated estimation of growth rate and associated trace element concentrations, most notably the Sr partition coefficient (D_{Sr}). First, we assumed a classical model for Sr partitioning behavior, and because Sr/Ca is affected by PCP, we modulated this value by Mg/Ca assuming congruent dissolution of bedrock (assuming negligible soil-derived components), and therefore equivalent bedrock and drip water chemistry (Stoll et al., 2022b; see supplemental methods). The resulting estimate for D_{Sr} can be directly correlated with growth rate, or background-subtracted (de-trended) to account for changes in baseline Mg (Fig. S3) and to record changes in amplitude (i.e. seasonal variation). An easier method of estimating this value is to calculate the ratio of Sr/Mg, which is directly proportional to D_{Sr}, assuming direct lattice partitioning of the divalent cations (i.e. no defect-driven particle incorporation). Importantly, annual layers with a thickness less than ~3 times the laser spot diameter are removed from this correlation, as integration of thinner layers by the laser leads to signal smoothing which necessarily leads to lower amplitudes correlating with slow growth. Also, given the potential for large variations in Mg/Ca due to crystallographic effects (Sliwinski and Stoll, 2021), areas of analyses were selected from stalagmites that demonstrated no anomalous fluorescent fabrics.

Wavelet analysis, in particular cross wavelet coherence analysis, was performed using the MATLAB-based algorithm developed by Grinsted et al. (2004) on Sr and Y waves (using MATLAB release 2020b) after removing spikes (i.e. values above the 99th percentile). To supplement this, a moving Pearson correlation coefficient was calculated in MATLAB between Sr/Ca and Y/Ca using a window of ~400 μm.

3.6. $\delta^{13}C$ and $\delta^{18}O$ analysis by isotope ratio mass spectrometry (IRMS)

Carbon and oxygen isotope samples were prepared by drilling powders from the mounted stalagmites at 0.2–1.0 mm resolution with a microdrill apparatus at ETH Zürich. A subsample of 90–140 μg was measured on a Thermo-Finnegan Delta V Plus mass spectrometer coupled to a Gas Bench II following the methodology of Breitenbach and Bernasconi (2011). Samples were bracketed by the in-house MS-2 (Carrara Marble) and Isolab B (ETH-2; Bernasconi et al., 2018) standards, which are regularly calibrated against NBS-18 and NBS-19 IAEA standards. Results are reported in permil relative to the Vienna Pee Dee Belemnite standard (VPDB), with typical analytical uncertainties (1 SD) of ±0.09‰ for $\delta^{13}C$ and ±0.10‰ for $\delta^{13}C$ based on the reproducibility of the calibration of the NBS standards.

4. Results

4.1. Drip water trace element data

Drip water data from La Vallina demonstrate two key points. First, with average stalagmite Sr/Ca values between 0.03 and 0.08 mmol mol^{-1} in monitored stalagmites (Table 1), and corresponding drip water ratios between 0.4 and 0.9, estimates for D_{Sr} can be obtained which range between 0.07 and 0.09 (Table 2). This is of the same magnitude as values derived by correcting Sr/Ca for PCP (Fig. 5), which typically range between 0.06 and 0.15 in fossil stalagmites. GUI is again an exception, with a drip water-derived D_{Sr} (0.19; Fig. 5; Table 2) about twice as large as the LA-ICP-MS-derived D_{Sr} (~0.1). This sample, however, also shows exceptionally high Ca concentration at the time of monitoring (~100 μg g^{-1} vs ~40 μg g^{-1} in other monitoring sites), suggesting higher solution saturation.

Second, drip water Y concentrations paired with drip rate estimates constrain the yearly Y delivery (μg yr^{-1}), and the relationship between this delivery and the total Y incorporation (deposition) into the stalagmites demonstrates a negative correlation with drip rate (Fig. 11; Table 2). An Y delivery is estimated for each drip site, amounting to ~0.7–5700 μg yr^{-1} using average drip rates and drip water Y concentrations from January and February

2021 (Table 2, Fig. S4; see Kost et al., 2022). Yttrium deposition in the stalagmites is calculated from growth rate (μm yr^{-1}), Y concentration (μg g^{-1}) and calcite density (g $μm^{-3}$), and amounts to 10^{-8} to 10^{-11} μg $μm^{-2}$ yr^{-1}. The ratio of each of these quantities (deposition/delivery) yields an estimate for trapping efficiency, which is negatively correlated with drip rate. For example, while SKY contains 10–100 times more Y than other active stalagmites, the estimated Y delivery is over 1000 times greater and the deposition/delivery ratio is correspondingly lower.

4.2. ^{14}C measurements and growth rates

All stalagmites collected under active drip sites (GUI, SKY, MUS, PLA and SNO) analyzed by AMS showed "modern" carbon (where $F^{14}C_{stal} > 1$), and a distinct peak corresponding to the acceleration and subsequent cessation of atmospheric nuclear arms testing in the 1950s (Genty and Massault, 1999) (Table S2). The location of the base of this peak (1959 CE) allows for growth rate estimates: All active stalagmites are growing relatively fast for this particular cave system, averaging between 70 μm yr^{-1} (PLA) and 320 μm/yr (SNO; Fig. S9). By comparison, fossil stalagmites record lower growth rates based on published U-Th dates, averaging ~20–60 μm yr^{-1} when hiatuses are excluded (Stoll et al., 2015; Stoll et al., 2013). Confocal fluorescence imaging reveals stretches of faster growth, though this is seldom faster than ~100 μm yr^{-1} (Fig. 2).

4.3. Fluorescence patterns

Distinct fluorescent layering is most prominent in fossil stalagmites (GUL, GAE, GAR, GEL; Figs. 3, S5), where typical growth layer widths are roughly consistent with U-Th-derived growth rates (Table 1). Active stalagmites demonstrate more ambiguous patterns (Fig. 2a–c, S5), and GUI alone displays robust and regular layering (Fig. 4). Here, comparison with the location of the ^{14}C bomb spike base (1959) confirms that these layers are, for the most part, seasonal. Among active stalagmites, SKY, MUS and SNO demonstrate complex fluorescence behavior, with ample evidence for

Table 2
Estimation of Yttrium flux and deposition rate (see Fig. 11) in comparison to Sr and D_{Sr}.

Sample	Drip rate [ml min^{-1}]*	Drip water Y [μg g^{-1}]	Stalagmite avg. Y/Ca [mmol mol^{-1}]	Y delivery [μg yr^{-1}]	Growth rate [μm yr^{-1}]	Y deposition [μg $μm^{-2}$ yr^{-1}]	Deposition/ delivery	Drip water Sr/Ca [mmol mol^{-1}]	D_{Sr}
MUS	3.0E+00	6.1E-06	7.3E−02	9.7E+00	1.5E+02	2.9E−11	3.0E−12	0.49	0.073
SKY	1.1E+02	1.0E−04	3.4E+01	5.7E+03	1.3E+02	1.2E−08	2.1E−12	0.46	0.074
PLA	3.7E−01	2.5E−04	3.9E+00	4.9E+01	6.6E+01	6.9E−10	1.4E−11	0.84	0.077
SNO	4.7E−01	3.5E−06	7.9E−01	8.5E−01	3.2E+02	6.8E−10	8.1E−10	0.61	0.090
GUI	3.4E−02	4.0E−05	2.4E+00	7.1E−01	1.8E+02	1.1E−09	1.6E−09	0.48	0.193

* Average of two points in Jan-Feb 2021; GUI estimated from 2009.

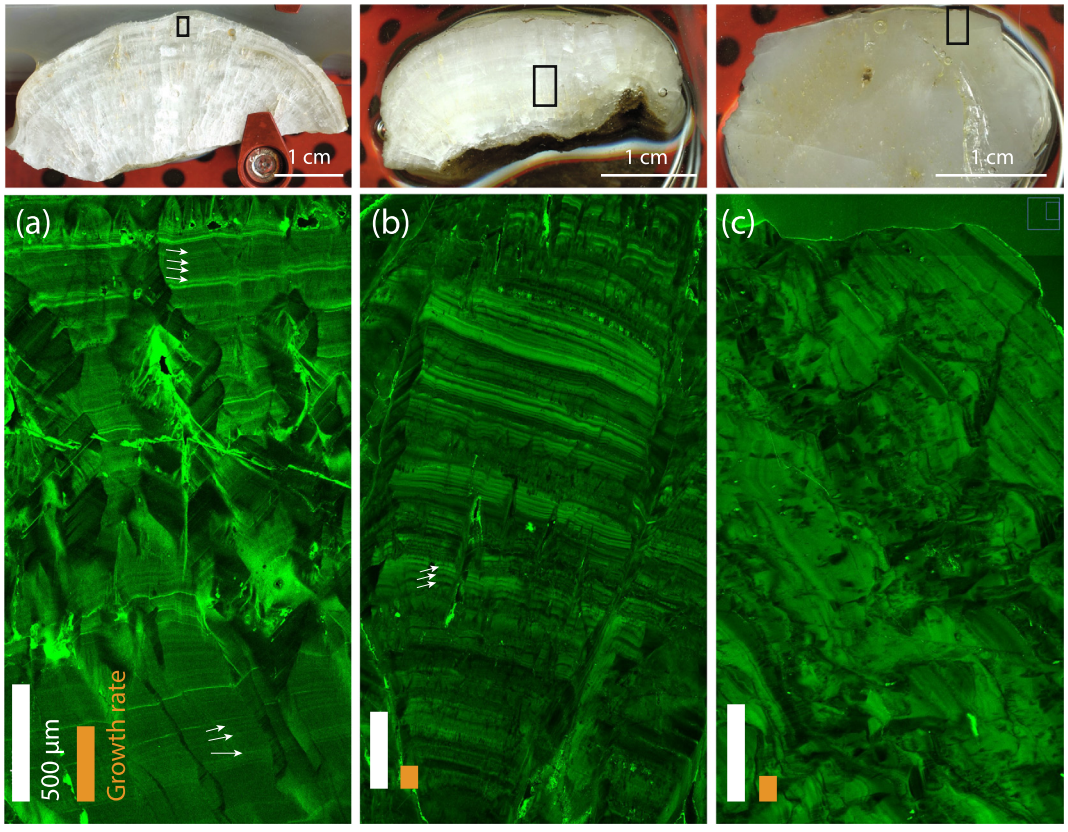

Fig. 2. Comparison of fluorescent features in active stalagmites: (a) SNO ("Snowball"), (b) MUS ("Mushroom") and (c) SKY ("Skyscraper"). PLA ("Playground") has poor fluorescence quality and is not shown here (see Fig. S5). White bars denote 500 μm, orange bars show the average growth rate of each stalagmite. White arrows show some of many visible sub-annual features. (top) inset in reflected light scans shows area of confocal imaging.

sub-annual banding (Figs. 2, S5). "PLA" displays very poor fluorescence with ambiguous evidence for seasonal banding (Fig. S5c).

The combined application of fluorescence imaging and trace element analysis shows, in nearly all cases, a close correspondence between bright fluorescent peaks and Y (Fig. 3). There are rare exceptions, with bright fluorescent areas lacking strong Y enrichment, as well as some mildly-fluorescent areas with pronounced enrichments.

4.4. D_{Sr} and Y/Ca vs growth rate

A relationship between D_{Sr} and growth rate can be evaluated in two ways, with growth rate estimated either by fluorescence banding or by trace element variations. Regarding the first, both GEL and GAR have long records of uninterrupted and distinct fluorescent banding, and the average growth rates in 100-year subsegments correlate with either average Sr/Ca, Sr/Mg or D_{Sr} (R^2 = 0.1–0.3; Fig. 5). In detail, GEL shows a significant correlation between growth rate and Sr/Mg and D_{Sr} ($P < 0.001$) and no significant correlation with Sr/Ca ($p = 0.55$). By contrast, GAR shows the reverse behavior with significant correlation between growth rate and Sr/Ca ($p < 0.001$) but only marginally significant correlation with the other two parameters ($p = 0.02–0.06$).

A similar effect can be demonstrated on a seasonal scale using trace element variations in stalagmites growing fast enough to properly resolve amplitude variations by LA-ICP-MS (i.e., GAL, GAE and GUI). Here, D_{Sr} correlates more significantly with growth rate (R^2 = 0.3, 0.3 and 0.1, respectively; $p < 0.0001$). The exact nature of this relationship differs between samples, and its linearity is only assumed. Regarding Y/Ca, a weak negative relationship with growth rate is observed in GEL and GAR (estimated by fluorescent banding; Fig. 6), and also in GAE and GUI (counted by trace element concentrations; GAL has a slight positive correlation).

4.5. Strontium and Yttrium correlation on multi-annual timescales

Fossil stalagmites and GUI (see Table 1) typically have Sr/Ca and Y/Ca ratios of 0.03–0.12 and 0.001 mmol mol^{-1}, respectively, which oscillate on both seasonal and inter-seasonal time scales. Seasonal oscillations and inter-seasonal oscillations are evident in wavelet coherence analysis (e.g. Figs. 7, S6). Two main features appear in these plots, both of which are marked by strong anti-phase between Sr and Y. First, there is typically a band of high coherence centered on the growth rate (20–100 μm yr^{-1}), which agrees with manually-counted growth rates (Fig. 5) and growth rates from radiometric methods (Table 1). Second, multiple sporadic cross-correlations appear at lower frequencies in fossil sta-

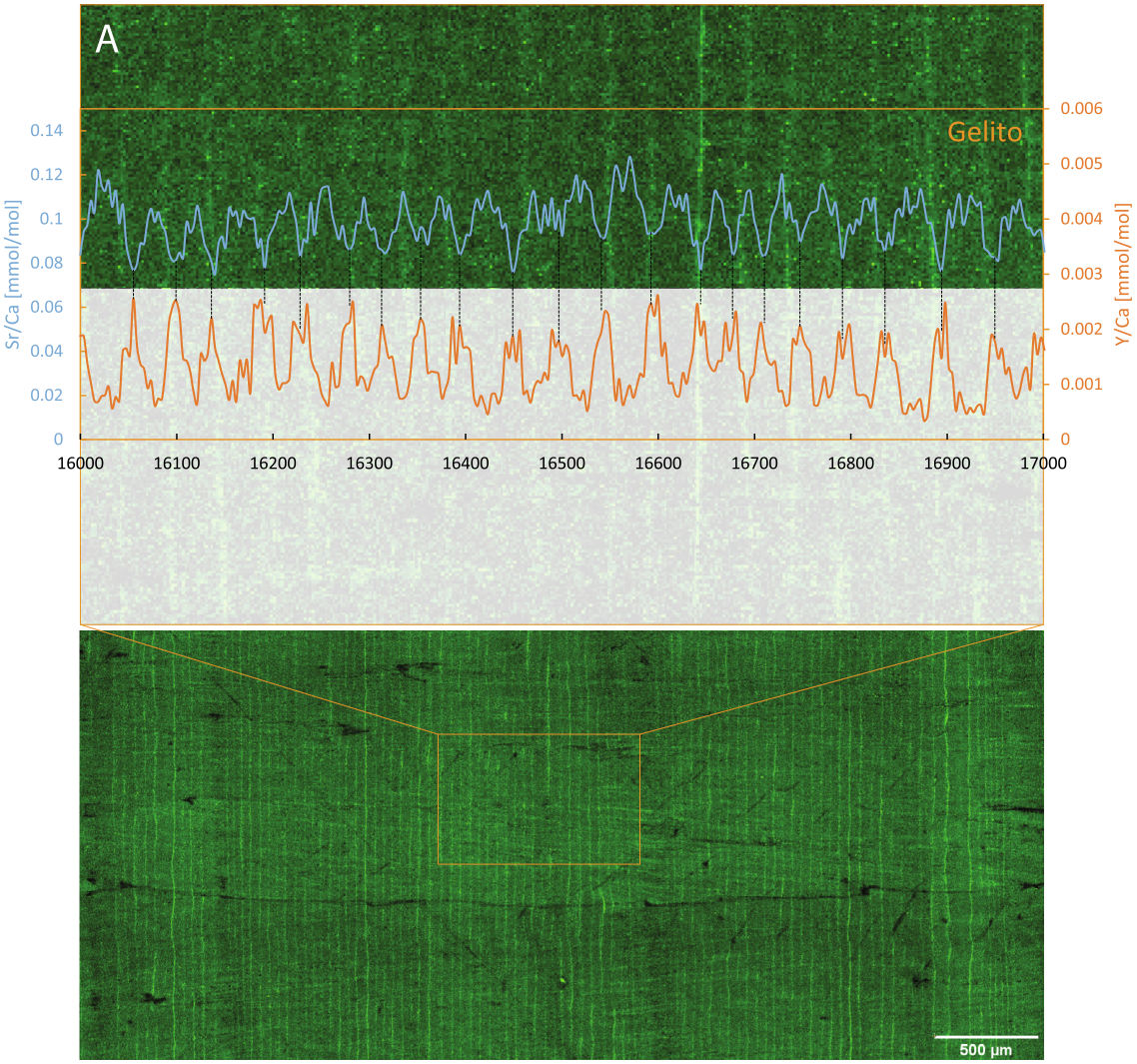

Fig. 3. Sr/Ca and Y/Ca covariation in GEL ("Gelito"), demonstrating consistent, long-term anti-correlation with Y peaks coinciding with bright fluorescent bands (confocal fluorescence image in backdrop). Horizontal axis demonstrates distance in μm, with the stalagmite growing to the left.

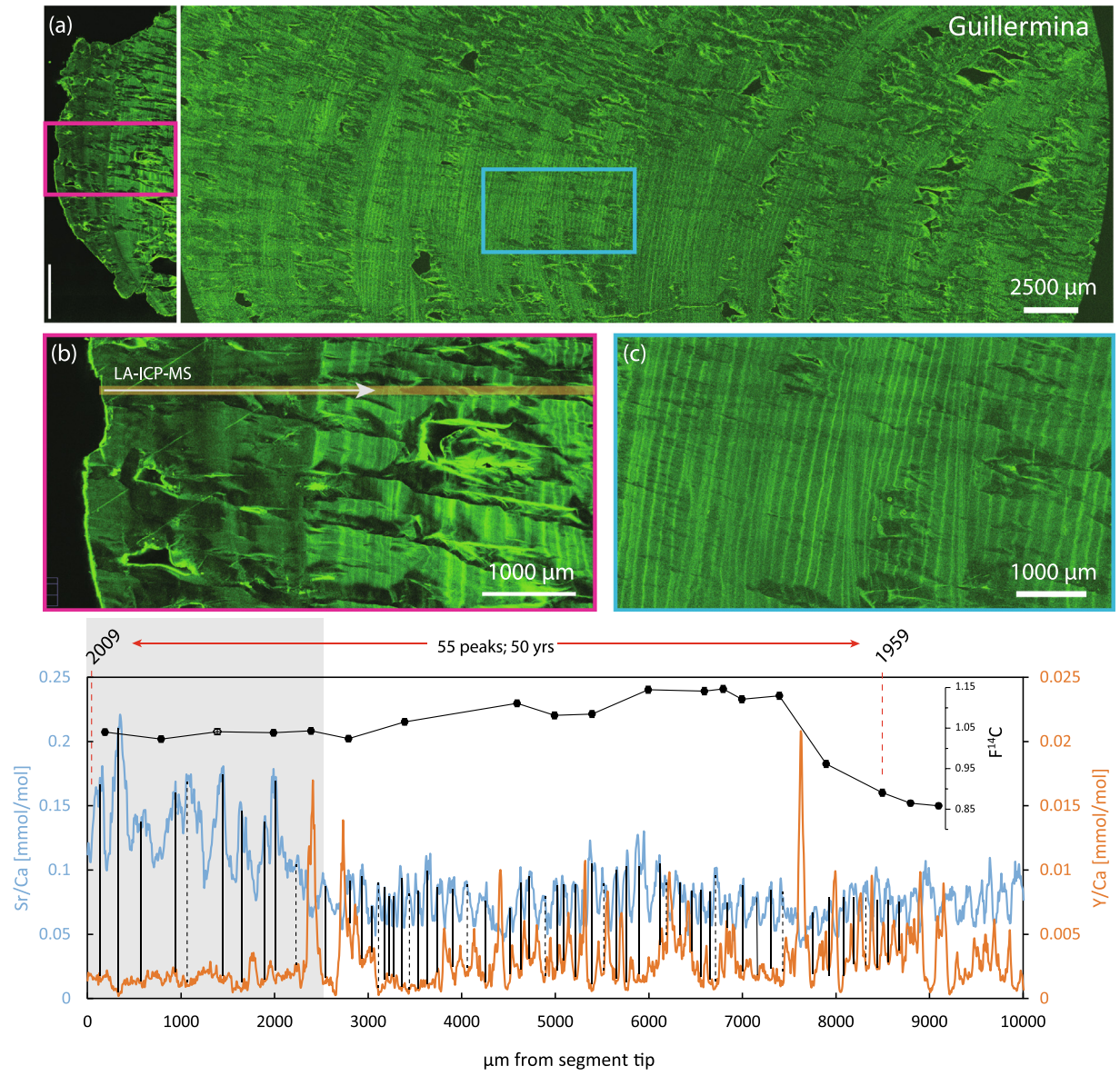

Fig. 4. Confocal and trace element concentrations from the tip of stalagmite GUI ("Guillermina"). (a) Overview confocal images (scale bar = 2.5 mm in both) with red and blue insets representing boxes (b) and (c) below. Note the loss of fluorescence banding near the tip (b), as well as regular seasonal banding throughout the rest of the stalagmite (c). (bottom): Sr/Ca increases, coincident with a loss of clear Y seasonality (grey box) in the region of fluorescence loss (b). Yearly cycles can be seen in Sr and Y concentrations, totaling 55 peaks between collection date (2009 CE) and the base of the bomb spike (1959) determined by $F^{14}C$ (bottom, inset).

lagmites, typically at 1,000–10,000 µm and corresponding to decadal to centennial time scales (note that the active stalagmites in this study are not old enough to resolve these time scales). Coherence between many low-frequency oscillations is less predictable than high-frequency oscillations and may demonstrate variation on multi-year timescales. They are, however, persistently anti-correlated.

These strong Sr-Y anti-correlations can be clearly seen in time-resolved records, wherein large negative Sr excursions are most often associated with simultaneous positive Y excursions (Fig. 8, top). This relationship can also be represented quantitatively in the form of a moving Pearson correlation coefficient, which demonstrates a largely negative relationship (Fig. 8, bottom). This marker tracks negative correlations not only in large-scale variations (e.g. GUL, GAE), but also in yearly covariations, where both Sr and Y concentrations anti-correlate but are relatively stable in the long term.

4.6. Active stalagmites

Active stalagmites generally show more complex fluorescence patterns and Sr-Y relationships than fossil stalagmites with less consistent R values than fossil stalagmites. However, growth rates can be estimated from bomb spike data, and trace elements can be compared with monitoring data and geographic/geological contexts.

Strontium-yttrium co-variation is typically complex but stable and largely consistent with fossil stalagmites, with Sr/Ca ratios averaging ~0.05–0.10 mmol mol^{-1} and Y/Ca varying more widely between 10^{-6} and 10^{-3} mmol mol^{-1} (up to 10^{-1} for SKY). Within a single stalagmite, Sr/Ca varies by as much as a factor of two, while Y/Ca may vary by orders of magnitude (Fig. 9, top). While waveforms are sporadically evident in one or both elements, wavelet coherence analysis reveals that the two elements are seldom oscillating at the same frequency, and if they are, they typically

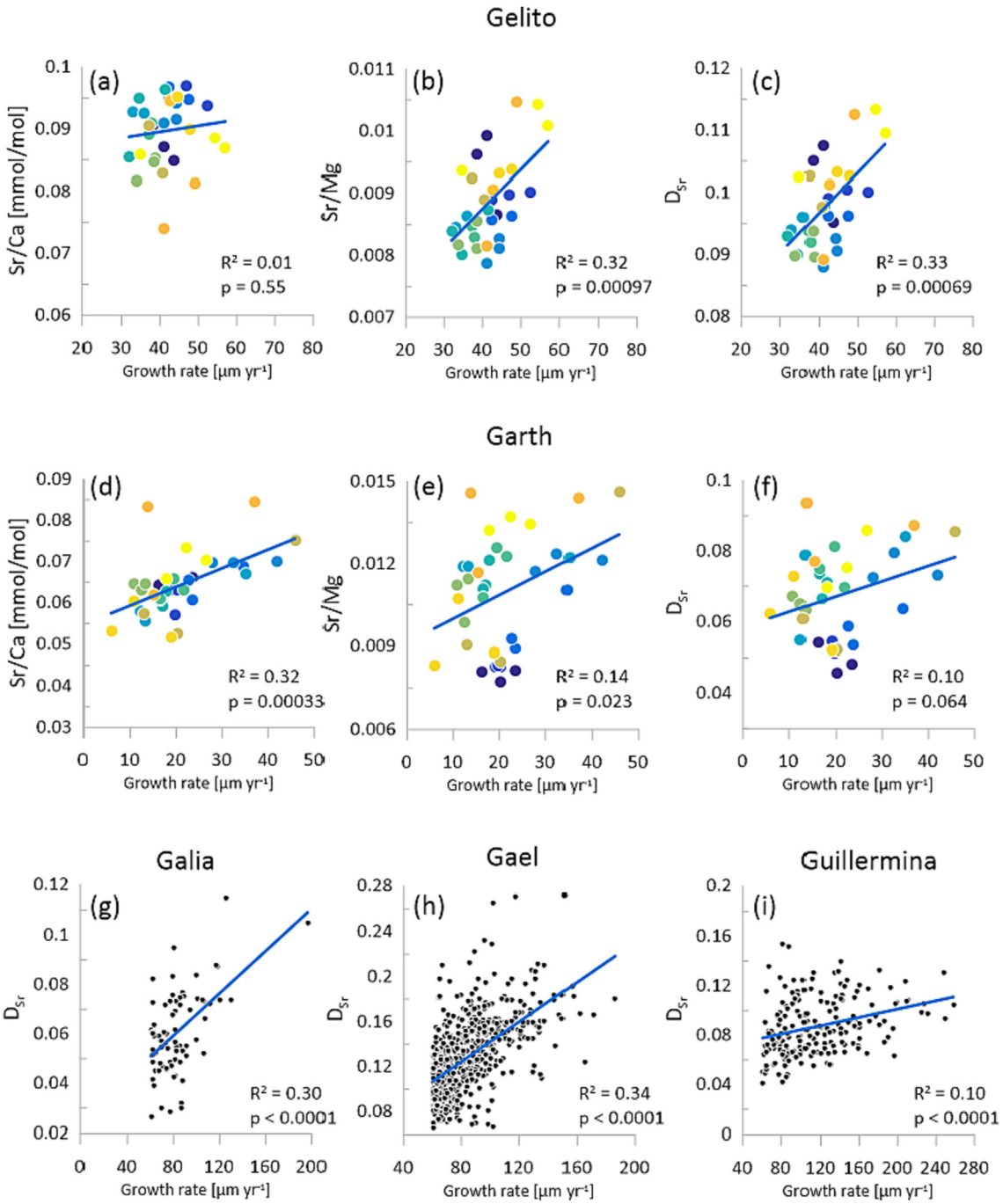

Fig. 5. Relationship between Sr/Ca, Sr/Mg, DSr and growth rate. (top, middle): GEL ("Gelito") and GAR ("Garth"), respectively. Stretches of ~3000 layers were counted to determine the growth rate 100 layers at a time. Chemical trends were averaged in these intervals. Note the general agreement between Sr/Mg and DSr. Coloring of points corresponds to distance along the stalagmite transect, with blue hues near the top and orange near the bottom. (g–i): Growth rate (µm yr^{-1}) vs background-subtracted D_{Sr} for GAL ("Galia"), GAE ("Gael") and GUI ("Guillermina"), where growth rates exceed 60 µm yr^{-1}. Growth rates determined as the distance between peaks, and correlated against the amplitude of D_{Sr} change.

have variable phase relationships (Figs. 7, S6). Moving Pearson correlation coefficients demonstrates irregular Sr-Y behavior in these four active stalagmites (Fig. 9, bottom).

GUI is notable in that the previously strong Sr-Y anti-correlation diminishes about 20 years before the collection date in the lower gallery (2009). The ratio Y/Ca drops, Sr/Ca increases to ~0.15 mmol mol^{-1}, and fluorescent banding disappears (Fig. 4), while $\delta^{13}C$ and $\delta^{18}O$ show distinct excursions: $\delta^{13}C$ decreases from −10 to −14‰, and $\delta^{18}O$ increases from −5.2 to −4.4‰ (Fig. 10). No comparable $\delta^{13}C$ and $\delta^{18}O$ records in this cave show similar excursions, including SNO (collected from near the mouth of the cave) and a host of other active stalagmites from the upper gallery (MUS, SKY, PLA).

5. Discussion

5.1. Prior assumptions

While a stalagmite's trace element budget is controlled in the latest stages by processes at the drip water-stalagmite interface,

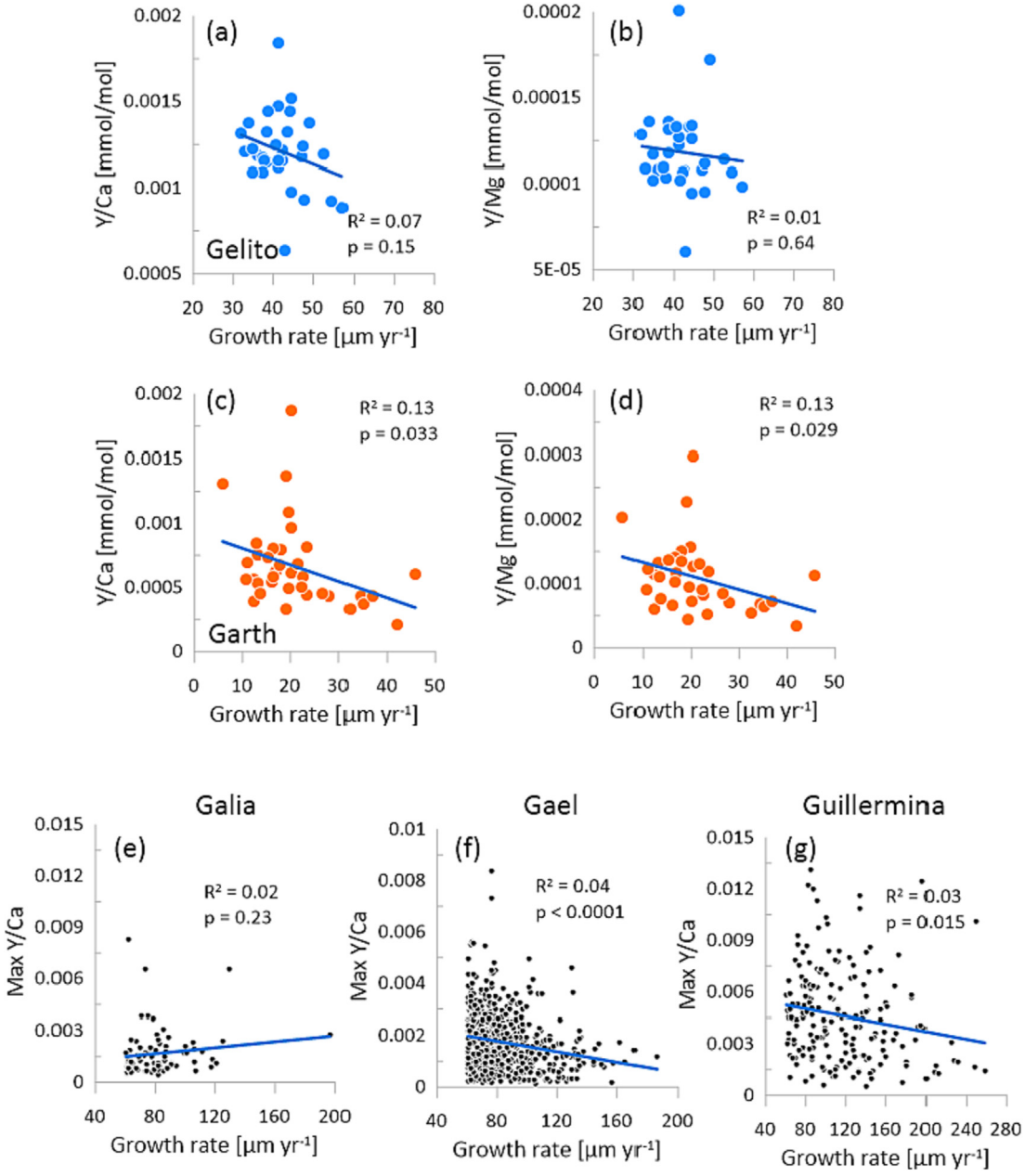

Fig. 6. Relationship between Y/Ca, Y/Mg and growth rate. (top, middle): GEL and GAR, respectively. Stretches of ~3000 layers were counted to determine the growth rate 100 layers at a time. Chemical trends were averaged in these intervals. Note the poor correlation between Y/Ca, Y/Mg and growth rate. (bottom): Growth rate [µm yr^{-1}] vs peak Y/Ca for GAL, GAE and GUI, where growth rates exceed 60 µm yr^{-1}. Growth rates determined as the distance between peaks, and correlated against the maximum Y/Ca in that interval.

the first-order controls are dictated by the chemistry within and around the karst system. The karst provides the background levels of most trace elements in drip water through dissolution of the bedrock, as well some of the organic matter (OM) that serves as a chelating agent for trace elements (Hartland et al., 2012). Exogenous sources of trace elements, such as sea spray, wind-blown dust and ash (both forest fire-derived and volcanic), percolate through both the overlying soil and the heterogenous karst system characterized by variations in porosity, fracture distribution, dolomitization and organic content, combining with karst waters to form the final drip water chemical and particulate/colloidal composition. As an added complexity, such exogenous inputs may be emplaced directly onto the stalagmite, forgoing dissolution into groundwater if the cave is sufficiently well-exposed. All of this complicates the interpretation of trace element signatures in stalagmites and underlines the importance of undertaking simultaneous drip water monitoring studies and making a few critical assumptions.

The first such assumption is that the modern drip water chemistry is representative of the entire history of the stalagmite. While monitoring is key to linking modern drip waters to their stalagmite equivalents, the process is laborious when undertaken at high resolution, and is typically not performed for more than a few years (e.g., Treble et al., 2015; Tremaine et al., 2016), capturing the most recent years of a stalagmite's growth. Meanwhile, linking fossil stalagmites to drip water data *requires* certain assumptions about composition and stability if trace element interpretations are to be made. The present study relies on drip water monitoring data provided by Kost et al. (2022) from La Vallina cave. These data

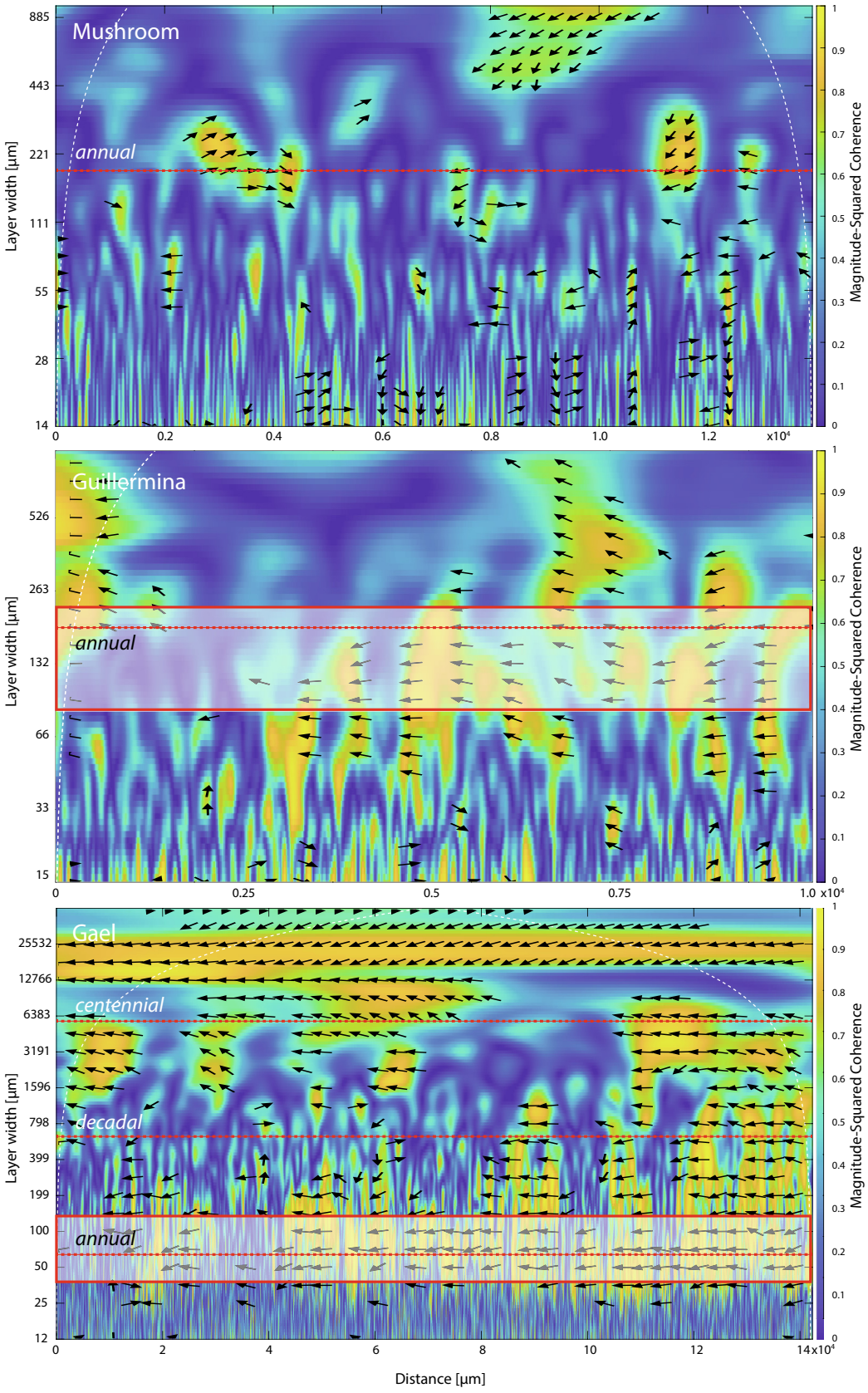

Fig. 7. Wavelet coherence analysis of MUS, GUI and GAE, demonstrating the strength of Sr-Y wavelet coherence on a length scale. The Y axis shows wavelet period, and shading represents the strength of correlation with yellow denoting higher strength. Arrows indicate phase of relationship: left = anti-correlation; right = in-phase correlation; up = Sr leads; down = Y leads. Note the lack of strong coherence in MUS, strong coherence between 60 and 260 µm in GUI (growth rate), as well as strong coherence in GAE at ~50 µm (growth rate) and strong anti-correlations at lower frequencies (inter-seasonal variations). Red boxes show typical growth rates (µm yr^{-1}), while dashed lines show typical annual, decadal and centennial cycle widths.

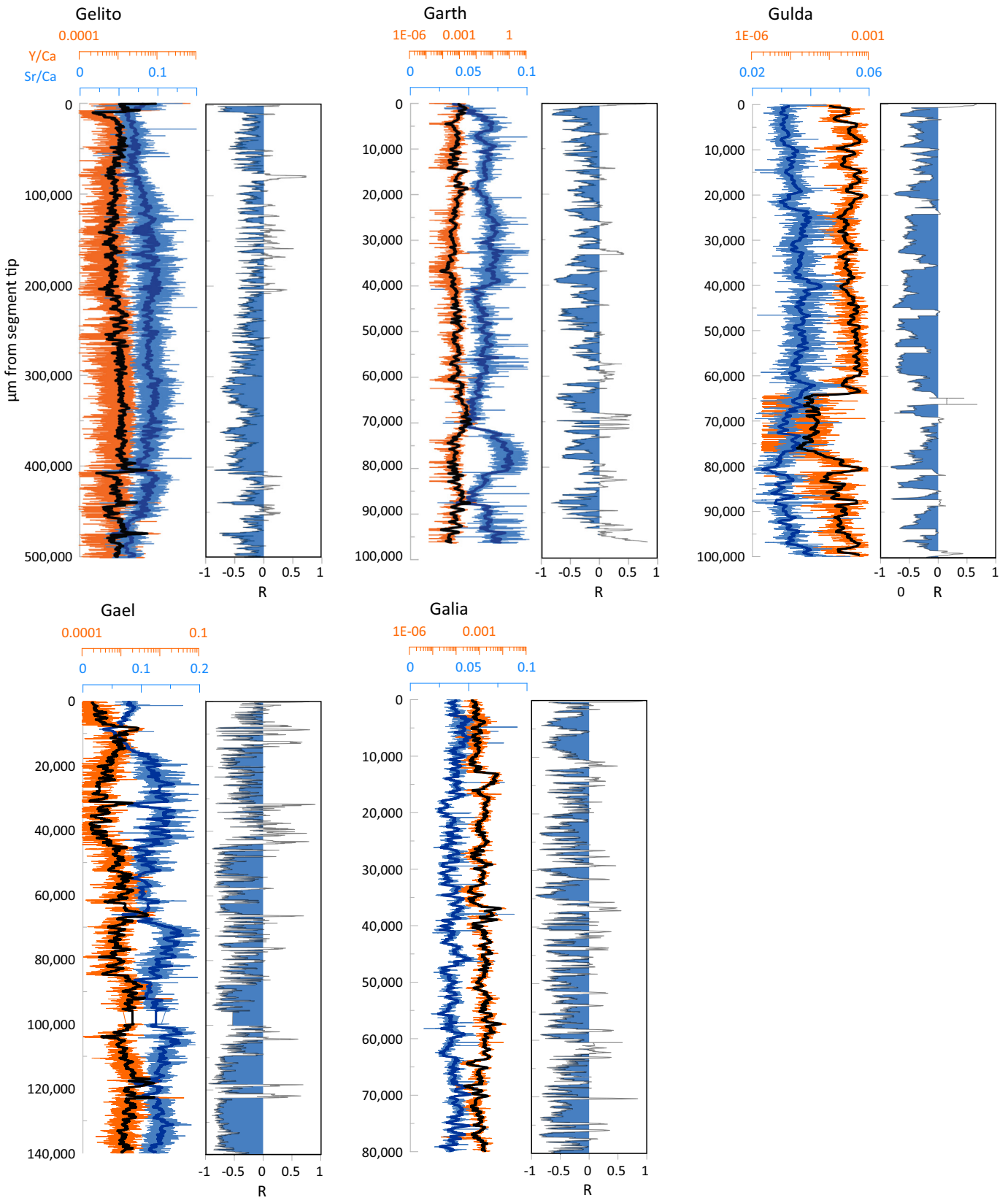

Fig. 8. Comparison of Sr/Ca and Y/Ca data for fossil stalagmites in La Vallina Cave. (bottom):, as well as moving Pearson correlation (R) for each stalagmite using a 100 point moving window (~400 µm), showing segments of negative correlation in shaded blue.

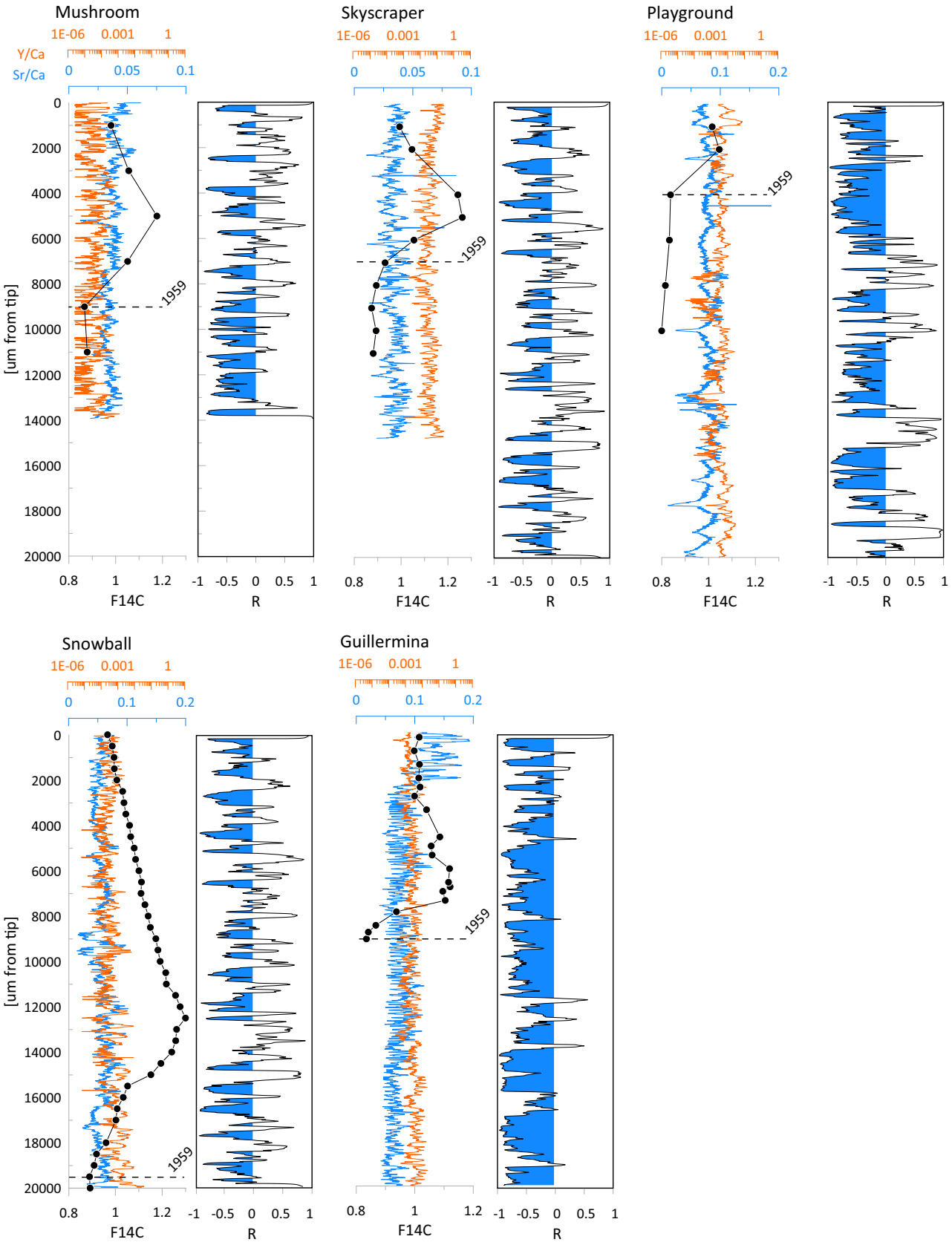

Fig. 9. Comparison of Sr/Ca, Y/Ca and $F^{14}C$ data (black points) for active stalagmites in La Vallina Cave, plotted against a linearly-interpolated age model (based on collection date and location of $F^{14}C$ bomb spike, see Fig. S9). (bottom): moving Pearson correlation (R) for each stalagmite using a 50-point moving window (~400 µm), showing segments of negative correlation in shaded blue. Dashed line indicates the base of the bomb spike (~1959 CE).

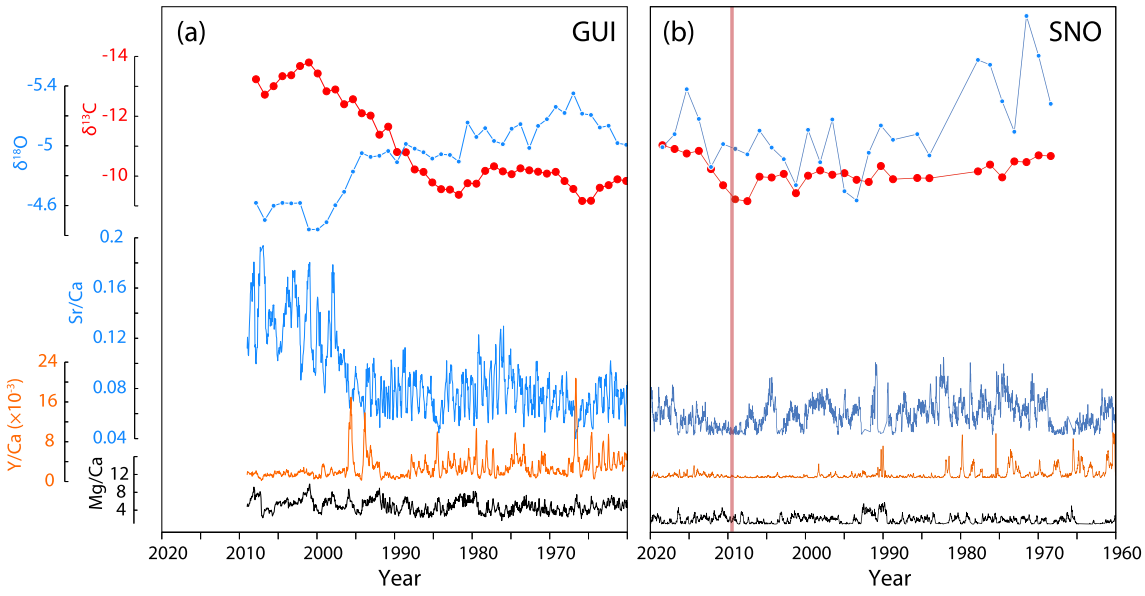

Fig. 10. Comparison of GUI (left) and SNO (right) $\delta^{13}C$, $\delta^{18}O$ and trace elements. Note that both series are plotted on the same y axes. Amplitudes of variation in trace elements are reduced in SNO, and there is no prominent $\delta^{13}C$ or $\delta^{18}O$ excursion (collection date of GUI marked with a yellow bar in SNO plot).

demonstrate seasonality and variability in drip water trace elements (Fig. S4), but at a lower amplitude and regularity than the same elements in stalagmites. We therefore assume that our observed trends in Sr and Y are predominantly caused by processes occurring at the stalagmite growth surface with subordinate influence from karst processes. Finally, we do not account for any exogenous input of Sr from particulate matter or soils. This assumption follows the generally poor association of Sr with colloidal organic matter (Hartland et al., 2012), the generally negative correlation between Sr and Al in all datasets (Fig. S10), and the geographic context in Asturias which limits the potential sources of dust input. Because we assume that all Sr is derived from the fluid phase and enters into the crystal lattice by substitution for Ca^{2+}, we maintain that the term "partition coefficient" (i.e. D_{Sr}) is appropriate for describing Sr incorporation (in the absence of soil, dust and sea spray contribution). Meanwhile, we continue to use the term "incorporation" for Y, given its complex partitioning behavior and low solubility.

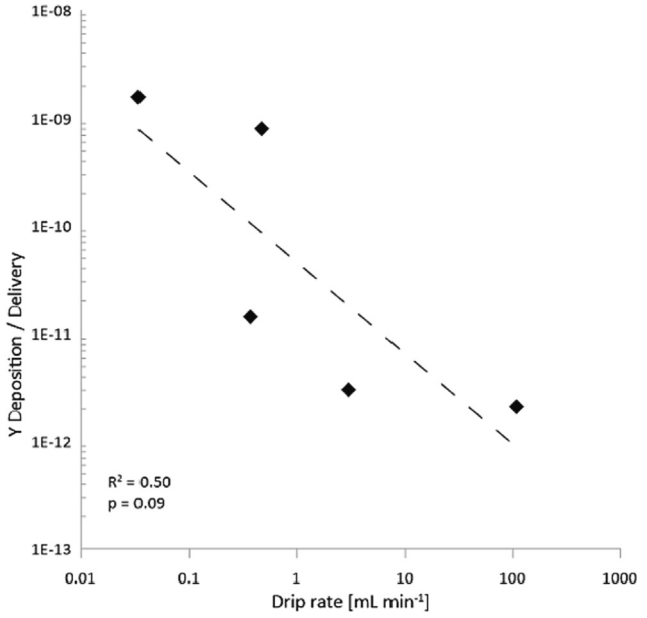

Fig. 11. Yttrium deposition (μg μm^{-2} yr^{-1})/Y delivery (μg yr^{-1}) vs drip rate (mL min^{-1}) for active stalagmites. Yttrium deposition calculated as the average Y concentration in each stalagmite over the last 50 years; Y delivery estimated from drip rate and drip water Y concentration (see Table 2).

5.2. Strontium partitioning correlated with growth rate and/or drip water supersaturation

Variations in Sr concentration, and therefore D_{Sr} were interpreted in earlier experimental studies to have a dependence on growth rate (Lorens, 1981; Teng et al., 2000; Tesoriero and Pankow, 1996), leading others to interpret that Sr maxima in stalagmites reflect periods of fast growth (Baker et al., 2014; Belli et al., 2017; Boch et al., 2011; e.g., Borsato et al., 2007), particularly when cave ventilation increases drip water saturation (Stoll et al., 2012). However, because Sr concentration is also a function of PCP, we employ a novel method of estimating D_{Sr}.

Namely, we estimate D_{Sr} from a number of stalagmites using coeval Mg/Ca and Sr/Ca ratios in high-resolution LA-ICP-MS transects where seasonality is clearly resolved (Fig. 5). Drip water monitoring data suggest relatively minor seasonal changes (<15%) in drip water Sr/Ca (Kost et al., 2022; Fig. S4), so we assume that larger variations (factor of 2) in stalagmite Sr/Ca are driven by a combination of growth rate and PCP. The latter is corrected with Rayleigh fractionation equations by assuming that the point of minimum Mg/Ca in a transect corresponds to the point of minimum PCP and maximum f_{Ca} (see Methods and Supplemental Methods). A similar estimate can be derived from a Sr/Mg ratio, which is directly proportional to D_{Sr} (Fig. 5) and simpler to implement than the iteratively calculated D_{Sr}. The latter quantity (D_{Sr}), while more familiar and transplantable into geochemical models, relies on a few key assumptions, most notably a constant bedrock-derived Sr/Ca and a point of maximum f_{Ca} corresponding to minimum Mg/Ca. The second assumption means that these values should be treated with caution, but they do fit well with more directly-measured distribution coefficients (Table 2) as well as literature values (Day and Henderson, 2013; Tremaine and Froelich, 2013; Wassenburg et al., 2020 and references therein).

The time-resolved D_{Sr} records correlate positively with growth rate, where growth rate is determined by either confocal layering (Fig. 5, top) or by trace element variations (Fig. 5, bottom). This relationship holds for a number of stalagmites growing in different time periods, suggesting a generality to the relationship, although it is not possible to extract a universal equation governing it given natural variations in bedrock Mg/Ca and Sr/Ca which are superimposed on the PCP record. This, together with potential variability in solution saturation, may explain the data scatter in Fig. 5. In particular, it is unclear if growth rate is directly responsible for differential Sr partitioning, as experiments by Wasylenki et al. (2005) suggest that *solution supersaturation* is actually the dominant factor controlling both growth rate and D_{Sr}. In natural samples, saturation state can only be indirectly inferred from the growth rate in natural samples, as opposed to being directly controlled in experiments. Forward modeling allows for the illustration of how this relationship may vary and complicate D_{Sr} – growth rate correlations.

Namely, the model I-STAL (Stoll et al., 2012) implements equations from (Dreybrodt, 1999) and experimental data from Tesoriero and Pankow (1996) and Lorens (1981) to derive a relationship between linear growth rate and D_{Sr}. Because of the saturation state dependence of growth rate, this relationship can be re-parameterized as a saturation-dependent D_{Sr}. This evokes the surface reaction kinetic model of DePaolo (2011), wherein trace element and isotopic fractionation are dependent on the rate of net precipitation relative to the gross forward and backward reactions (both dependent on saturation state). The relationship between saturation-dependent D_{Sr} and growth rate displays variable slopes and intercepts depending on the saturation state used, which in turn depends on soil pCO_2 (Fig. 12a). In natural samples, this would suggest that D_{Sr} calculated across periods of significant climate change with variable temperature and soil productivity would show positive correlations between D_{Sr} and growth rate, but the shape of these correlations would vary in a way that would ultimately add scatter to the data and decrease the correlation strength. For instance, the separation of Fig. 5f (GAR D_{Sr}) into segments counted from the top (blue) and bottom (orange) of the sample yields two distinct regressions, each more significant than the regression over the entire dataset (Fig. 12b). Given the shifting climatic conditions (glacial termination *T*-II; Table 1), it is justifiable to treat these segments separately, in a method employed by (Belli et al., 2017). Climate variation carries with it changes in cave ventilation regimes, which impart an indirect control on stalagmite Sr concentrations by modulating the drip water degassing rates and thereby the solution saturation states. That is, while seasonal cave ventilation should always follow yearly temperature variations, it is possible that the duration of the ventilated season could vary if atmospheric temperatures change faster than cave bedrock temperatures.

While correlations between Sr concentration and growth rate have been made in stalagmites (e.g., Belli et al., 2017), the point remains contentious because stalagmite growth/farming experiments have not demonstrated this relationship. Both Tremaine and Froelich (2013) and Wassenburg et al. (2020) used unseeded glass plates to precipitate calcite, wherein no Sr-growth rate relationship was observed. Both studies noted the poor constraint on low crystallization rates and possible nucleation effects that may hinder crystallization in unseeded experiments. Additionally, it's possible that the primary calcium carbonate to precipitate on an unseeded plate is not calcite, but another phase (e.g. amorphous calcium carbonate), which partitions trace element differently (Demény et al., 2016). Nevertheless, even seeded experiments produce ambiguous correlations (Day and Henderson, 2013; Huang and Fairchild, 2001), which suggests the relationship is not straight forward. Belli et al. (2017) noted that although lamina thickness (growth rate) was positively correlated with Sr concentration, the correlations contained a lot of scatter and necessitated the consideration of additional factors, such as infiltration rate which affects the fluid film thickness and potentially saturation state. It is unclear why the discrepancy exists between *in situ* measurements and experiments, but it is conceivable that the modest correlations seen by (Belli et al., 2017) and in this study (Fig. 5) are achievable predominantly when considering larger data populations (albeit with a lot of scatter). Alternatively, the discrepancy may be due to differences in how growth rates are estimated. In farmed calcite experiments, masses of calcite are measured, whereas in *in situ* studies, the growth rate is estimated from the vertical extension rate. It is possible that increases in solution saturation (brought about by changes in ventilation or hydrology) lead to localized increases in Sr uptake at the apex of the stalagmite, while the total calcite precipitated is conserved. This would generate more apical morphologies, which is most clearly seen in the morphology of GUI (Fig. 4) associated with a sudden spike in Sr concentration.

Two final caveats to the relationship between growth rate and D_{Sr} should be noted. First, layer counting yields only an *average* growth rate over the year, which may differ markedly from instantaneous growth rate. Seasonality in precipitation, temperature and bioproductivity plays a crucial role here: a year where stalagmite growth is restricted to a brief and intense period would record a high D_{Sr} (via the maximum Sr/Ca), but low overall growth rate

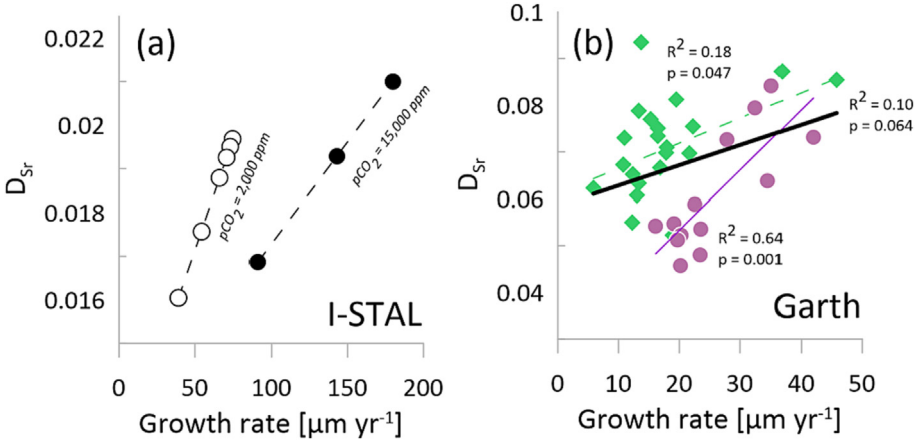

Fig. 12. Variable response of D_{Sr} to solution saturation: (a) calcite precipitating from two hypothetical solutions modeled in I-STAL with identical drip interval, bedrock chemistry and temperature, but variable soil pCO_2. Note that the response of D_{Sr} to growth rate differs between the two scenarios. (b) D_{Sr} vs growth rate in GAR (from Fig. 4), separated into two halves of the transect (circles = top; diamonds = bottom). Regressions for each half and the full data set suggest that the pairing of D_{Sr} and growth rate changes over time.

due to inactivity throughout the rest of the year. By contrast, a less seasonal year may record more overall growth, but without the same magnitude of D_{Sr} peak. Both correlations, while positive, would have different slopes and intercepts, and when summed together would produce a weaker correlation coefficient. The summation of this together with variability in saturation state and bedrock chemistry, may account for the variance in D_{Sr} vs growth rate correlations. Finally, it should be emphasized that such analyses are restricted to stalagmites that either have consistent, well-defined fluorescent layers and/or consistent trace element cycles >60 μm yr^{-1} (i.e., 3 times the laser spot size). This includes most of the fossil stalagmites in this study (GEL, GAR, GAL, GAE), and one active stalagmite (GUI). GUL demonstrates little variability in slow-growing layers, while active stalagmites demonstrate rapid growth with unpredictable yearly Sr-Y patterns.

5.3. Yttrium transport and relation to infiltration

Fluorescence patterns in stalagmites are consistent with literature interpretations of fluorescence being associated with organic matter (Orland et al., 2009; Perrette et al., 2005; Shopov, 2009; Sliwinski and Stoll, 2021) and organic matter being associated with colloidally transported elements (Borsato et al., 2007; Hartland et al., 2012; Orland et al., 2014; Pearson et al., 2020). As a highly-insoluble high field strength element, Y depends critically on colloids for transport through the karst, and it is unclear if it incorporates into calcite as a free ion or as a complex with its colloidal host. Hartland and Zitoun (2018) demonstrated that the availability of free Cu^{2+} in solution could be as much as five orders of magnitude lower than the true concentration if organic ligands were involved in complexation, and it is likely that similar factors affect elements like Y. Given the low abundance of Y in drip water and the likelihood that the concentration of *free* Y^{3+} is much lower, it is likely that Y incorporation occurs either together with its colloidal host, or upon dissociation from it at the stalagmite surface. Indeed, Y and geochemically analogous REE are readily incorporated into the calcite lattice (Qu et al., 2009; Terakado and Masuda, 1988; Voigt et al., 2017), a process that is aided by their complexation in solution (Sawada et al., 2005). If this complexation is provided by DOM, then Y behaves similarly to elements like Co, Ni and Cu, which are susceptible to removal by PCP unless chaperoned by a ligating agent (Lindeman et al., 2021). Their incorporation into the calcite lattice then becomes a function of the element's lability, i.e. the rate of dissociation from DOM (Hartland et al., 2014).

The association of Y with Zn, Cu and Pb led Borsato et al. (2007) to speculate that Y was recording the delivery of heavy autumnal infiltration in the cave, a notion that was supported by other studies noting the sudden flux of dissolved organic matter in the autumn (Baker and Genty, 1999; Baker et al., 1999), or influx of organics during wet months in drier climates (e.g., Orland et al., 2012). The connection of this effect to seasonal Y peaks in stalagmites is, however, difficult. Baldini et al. (2012) demonstrated in Ballynamintra Cave (Ireland) that peak drip water Y concentrations were recorded during summer months, *prior* to heavier autumnal infiltration, and Fairchild et al. (2010) made a similar observation in Obir Cave (Austria) that drip waters in high-infiltration months did *not* supply trace elements at a proportionally higher rate to explain stalagmite chemical variations. Similarly, in this study we find that stalagmite Y concentrations can vary by several orders of magnitude within one year (e.g. Fig. 4), while drip water Y concentrations typically vary by one order of magnitude (Kost et al., 2022; Fig. S4). The incorporation of Y in discrete peaks is therefore most likely controlled by crystallization processes rather than flux, and we propose a conceptual model to describe this process.

5.4. Conceptual model for Y incorporation into stalagmites

Namely, we propose a model to explain Y variation in stalagmites based on three overlapping effects, and assume an exclusive delivery to the stalagmite surface via organic colloids (Hartland et al., 2012):

1. Retention: Y incorporation is maximized when its host colloids have sufficient time to bind to the stalagmite surface, allowing Y to dissociate and then incorporate into the calcite, or allowing the colloids to incorporate together with their trace element load. In either case, low drip rates lead to better overall incorporation.
2. Dilation: Rapid growth (fed by high saturation state) distributes an otherwise constant Y flux over a longer distance, generating lower average concentrations in fast-growing segments (as measured by LA-ICP-MS).
3. Delivery: Y is controlled at the source by drip water concentrations and drip rate, with higher drip rates effectively diluting the Y concentration.

Following observations by Fairchild et al. (2010), Baldini et al. (2012) and drip water monitoring in La Vallina (Kost et al., 2022; Fig. S4), we propose that drip water Y delivery (3) is much smaller than the variations seen in the stalagmite record, and this effect is therefore subordinate to crystallization dynamics. While there appears to be some seasonality to the drip water Y concentration, the noisiness of the time series and the tendency for large transient spikes randomly throughout the record seems at odds with the relative consistency seen in stalagmite Y record. We therefore explore the first two effects in more detail but maintain that the amount of colloidal matter delivered to the stalagmite must necessarily play a role as well.

5.5. Retention efficiency

Concerning the first effect (retention), we propose that the incorporation of Y and/or colloids into stalagmites requires sufficient surface residence time associated with low drip rates, as well as sufficient water to transport the colloids (i.e. deposition cessation in the summer precludes colloidal incorporation). Such conditions are met during the limited transitional period from dry to wet conditions in the autumn, which explains why yearly Y concentration profiles can vary by up to an order of magnitude, while more soluble elements (e.g., Sr) oscillate between two semi-consistent values. Summertime calcite precipitation is not discounted in this model: while a shift from dry to wet conditions favors Y and colloidal incorporation, a shift from wet to dry conditions in the spring may do likewise. Because a double fluorescence peak from this hypothetical scenario is typically not observed, it is likely that the two maxima in colloidal delivery are condensed into a single layer, wherein intervening summertime growth is minimal. Support for the retention model comes from comparison of drip water monitoring data. Using average drip rates and Y concentrations at five monitoring sites, a yearly Y delivery can be estimated (Table 2), and the average stalagmite Y concentration divided by this number provides an approximation of retention efficiency (Y incorporation/delivery; Fig. 11). The data suggest that while stalagmites under faster drips have higher average Y concentrations, this quantity is outpaced by the increase in Y delivery, and stalagmites under faster drips retain less of the delivered Y.

Multiple studies have examined the incorporation of organic matter into stalagmites, both in natural samples incorporating humic and organic acids (Lindeman et al., 2021; Pearson et al., 2020) and in synthetic calcites incorporating fluorescent dyes (Green et al., 2016; Marzec et al., 2018) and other organic matter

(Cho et al., 2016; Kim et al., 2011). One prevailing paradigm in experimental studies is that organic incorporation is dictated by the kinetics of adsorption/desorption (Kim et al., 2019), and is most effective when desorption is limited (e.g., Chalmin et al., 2013). In stalagmites, desorption of organics occurs when a new drop flushes away a film of accumulated organic compounds. In summer months with low drip rate, desorption is low, favoring colloid (and Y) incorporation, but growth is moisture-limited. Meanwhile, high drip rates in winter months maximize desorption and prevent Y incorporation and calcite concentrations are biased to include higher amounts of Na, Mg, Sr (Sliwinski and Stoll, 2021). Autumn months in these scenarios would be ideal for preserving an Y input, as two conditions are met: moisture is beginning to enter the system due to shifting weather, but not to the extent that organic colloids are desorbed from the surface. While Borsato et al. (2007) suggest similar timing for fluorescent banding, they interpret the banding as the result of organic flushing from the soil as opposed to autumnal optimal depositional conditions described here.

While the Y^{3+} ion is highly compatible in the calcite lattice, it likely must first desorb from its colloidal host before incorporation (Hartland et al., 2014). Otherwise, it may incorporate directly with its colloidal host. Distinguishing these two effects is complex because lattice-bound Y^{3+} would remain in the vicinity its colloidal host if desorbed and incorporated into calcite. It should be noted that the presence of DOM is inferred from the fluorescence of the calcite, although as noted by Perrette et al. (2005), this fluorescence may be related to the porosity of the calcite fabric. If so, the porosity is anyway associated with an increased internal surface area which increases DOM binding probability. This and other fabric-related changed caused by DOM (Pearson et al., 2020) are indeed quite difficult to discern in fluorescent bands that are <5 μm in width. It is equally difficult to discern whether slow growth promotes DOM retention, or DOM slows calcite growth as suggested by Pearson et al. (2020), although the argument can be made that water limitation in the summer is a stronger control on growth rate.

5.6. Yttrium dilation in stalagmites

Concerning the second effect (dilation), the regular yearly cycles result from an Y flux which is variably dilated and condensed within the stalagmite depending on the instantaneous growth rate. For example, a doubling in Y concentration between a peak and trough (e.g., Fig. 3) could be explained by a halving of the growth rate, such that the product of the two would be constant throughout the year (assuming constant Y input). While determining the instantaneous growth rate in a single year is prohibitively difficult, support for this model can be found by examining long-term Y-Sr correlations (Fig. 8), wherein the two show persistent anti-correlation. Qualitatively, major dips in Sr are correlated with peaks in Y and vice versa, and this is echoed by wavelet coherence analysis which shows anti-correlation on annual, decadal and centennial time scales. Therefore, if one assumes that Sr/Ca is proportional to the growth rate, then it follows that Y is inversely proportional to the growth rate, and dilation is therefore a controlling factor on its concentration.

While the Sr-Y anti-correlation in fossil stalagmites is strong, it is notably variable in some segments (Fig. 8), suggesting that either dilation is not singularly responsible for Y variations, or that Sr is not as directly correlated with growth rate. This will be explored further when discussing active stalagmites (*section 5.7.).* Furthermore, both of these models assume that Y is sourced entirely from organic colloids, which is complicated by demonstrable associations of Y with detrital matter or with elements which are predominantly associated with detrital particles (e.g., Fairchild and Treble, 2009; Zhou et al., 2008). Even so, the preceding discussion presents a framework for the interpretation of trace element signatures in a number of samples in this study.

5.7. The effects of vegetation on stalagmite trace element and isotope records

Because GUI was active at the time of collection, its trace element and isotopic variations can be tied to known changes in local climatic and hydrological conditions. Here, Sr and Y oscillate regularly over much of last ~400 years (Fig. 4), except in the interval 15–20 years before collection, wherein the characteristic anti-correlation and fluorescent banding are lost, and Sr/Ca increases by a factor of two (Fig. 4). The local context and chemical/isotopic trends are important for interpreting these changes. GUI is located in the lower gallery, which is strongly ventilated by a combination of incoming cold winter air and periodic strong advective ventilation by a stream. The drip rate above GUI is notably slower than other active stalagmites (Table 1), and we explore the possibility of a relation with land use. While the exact nature of the land use in past centuries is also unknown, the presence of old stone walls and stables suggests that it was previously used as livestock pasture. The forest above GUI is now dominated by planted eucalyptus trees (replacing the native *Quercus),* which are <90 years old based on trunk diameters (Ferrere et al., 2005). Importantly, the roots of the eucalyptus can be seen infiltrating the roof of the cave, and this may be reflected in $\delta^{13}C$ and $\delta^{18}O$ records. Namely, the pronounced negative $\delta^{13}C$ excursion in the stalagmite may instead be due to tree planting into formerly pastoral land, thereby increasing CO_2 supply through deeper roots and generating a negative $\delta^{13}C$ signature (e.g., Meyer et al., 2014; Treble et al., 2015). The positive $\delta^{18}O$ excursion may be explained by the same processes, as increased evapotranspiration would drive percolating drip water $\delta^{18}O$ to more positive values. Other active stalagmites from the same cave system show no comparable Sr excursions (Fig. 9), suggesting that regional air temperature changes are not responsible for the shifts, and this is especially true for SNO, where $\delta^{13}C$ additionally shows no excursion (Fig. 10). The lack of $\delta^{13}C$ excursion in SNO also rules out the Suess effect, which would affect all stalagmites, and account for a maximum of ~1‰ offset in the decades between 1960 and 2010 (Genty and Massault, 1999). Finally, Mg/Ca ratios in both GUI and SNO do not suggest any change in PCP in this period that could account for shifts in Sr. Given this context, recent Sr-Y systematics can be explained in several ways:

First, because the timing of this chemical excursion is coincident with hypothesized land use changes in the area (with eucalyptus trees planted to provide fast-growing raw material for the paper industry), the change in foliage may have impacted the soil biogeochemistry. Eucalyptus foliage is known to inhibit microbial community growth (Briones and Ineson, 1996) and does not senesce and degrade in the same manner as native oak species and other deciduous trees. Rather, the species relies on forest fires to promote germination and eliminate competition, and to this end it releases slowly-degrading and oily and foliage that becomes highly-flammable when dry (Dos Santos et al., 2015). A shift from deciduous oak-dominated foliage or pasture to eucalyptus in the last decades is consistent with a decreased rate of organic colloid delivery recorded in both fluorescence loss and Y decrease (Fig. 4), as well as a Sr increase (i.e. less Sr inhibition by organic colloids). One should note, however, that Sr oscillation is preserved in this time period, indicating that seasonal cycles in ventilation and pCO_2 may still be controlling drip water oversaturation, growth rate and Sr incorporation, or that seasonal cycles in colloidal input are nevertheless present.

Second, autumnal rainfall could have decreased in intensity in the past decades, decreasing the flux of colloids and Y, while aiding the incorporation of Sr. While precipitation records from Asturias

and Cantabria show some decrease in precipitation in the 1980s relative to previous decades (Esteban-Parra et al., 1998), the magnitude of this change is similar to changes in prior decades which are *not* associated with a sudden Sr increase in GUI. A variant on this explanation relates to changes in P-ET (precipitation minus evapotranspiration): greater vegetation cover increases evapotranspiration, reducing the P-ET and effective infiltration into the cave, thereby decreasing the amount of colloids transported. This latter hypothesis is consistent with vegetation recovery, although it should be noted that Sr cycles in these last decades show very fast growth, which is inconsistent with lower infiltration.

Finally, yttrium concentrations may be reduced by dilation, as noted above (Section 5.5). The δ13C record over the past decades suggests enhanced soil/root respiration and increased drip water saturation, which is corroborated by an increase in growth rate in this interval and increased Sr/Ca and D_{sr} (Fig. 4, Table 2). The dilation effect can be tested in a simple way by examining the average Y/Ca over intervals of variable growth rate. In the uppermost 2.2 mm (~20 years) GUI is growing at ~220 μm yr^{-1} and records an average 0.0016 mmol mol^{-1} Y/Ca. In the preceding decades, Y/Ca is approximately double (0.0032 mmol mol^{-1}), with a growth rate slightly more than half (~138 μm yr^{-1}), making this a plausible explanation. It additionally poses a critical question: given that similar Sr excursions are seen in the fossil stalagmite record where eucalyptus was *not* present (Fig. 8), is there an alternate explanation for the preceding trends that excludes eucalyptus altogether? Perhaps the most prominent feature of the eucalyptus trees in this study is the root system that infiltrates the cave, which can by itself explain the trends in $\delta^{13}C$, $\delta^{18}O$ and trace elements (Meyer et al., 2014). If this is the case, then similar Sr shifts in fossil stalagmites may reflect either (1) periods of reforestation, or conversely, deforestation driven by short-lived climate events; or (2) other changes in infiltration pathways related to the opening and closing of feeding fractures not directly related to root systems.

5.8. Sr-Y correlation in active and fossil stalagmites

The persistence of Sr-Y anti-correlation (e.g. Figs. 6–8) is noteworthy and suggests that their incorporation is linked. Similar patterns of seasonal covariation in Grotta di Ernesto cave led Borsato et al. (2007) to speculate that Sr incorporation is inhibited by high dissolved organic matter (DOM) flux (Baker et al., 1999; Frisia et al., 2003), consistent with experimental work performed by Chalmin et al. (2013). Alternately, the correlation may be indirectly linked to the complex interplay between cave ventilation, drip rate and solution chemistry, as noted above. For instance, fast growth generates high Sr concentrations while simultaneously decreasing Y by dilation on a decadal to centennial scale. Simultaneously, fast drip rates lead to fast growth (high Sr) while decreasing Y retention times. However, the superposition of several processes opens the possibility that certain effects counteract each other, as demonstrated by certain active stalagmites.

Most notably, four of the five active stalagmites in this study (MUS, SKY, PLA and SNO) demonstrate irregularity in Sr-Y anti-correlation with respect to the fifth (GUI), including an unpredictable moving Pearson correlation coefficient (Fig. 9), poorly defined waveforms (Figs. 7, S6), as well as complex fluorescence patterns with unclear seasonality (Figs. 2, S5). Three of these (SKY, MUS and PLA) were located under active drips in the summer, suggesting that these sites likely received colloidal matter during drier months where retention efficiency was higher. This may be responsible for these stalagmites' highly complex fluorescence patterns: because colloids in this scenario are delivered throughout the summer as opposed to at the start of autumn, many more fluorescent bands are expected, and the corresponding Y concentrations would not be strongly anti-correlated with Sr in these time periods because the of poor cave air ventilation. GUI is spared from this effect by its slow drip rate which ceases in the summer. The summation of these observations suggests that periods of poor Sr-Y anti-correlation in a stalagmite with otherwise predictable Sr-Y behavior represent times of increased summer drip rate, possibly through a change in flow regime from a diffuse flow to a fissure flow (Baldini et al., 2021), which may or may not be related to more global climate shifts.

For instance, fossil stalagmites in this study show strong, persistent anti-correlations between Sr and Y, interspersed with periods of poor anti-correlation (Fig. 5), suggesting that there are periods where seasonality in colloidal delivery/incorporation or ventilation are disrupted, and Sr-Y correlation strength may serve as a proxy for shifts in local climate. A shift towards warmer winter and summer temperatures in the last decades is consistent with disruptions of regular cave ventilation patterns, which would affect Sr oscillations in active stalagmites by hindering winter deposition (with an exception of GUI). At the same time, a shift to a wetter summer may likewise provide more summertime infiltration, which would simultaneously increase both Y and Sr and complicate any pre-existing anti-correlation.

Finally, strong Sr-Y inter-annual covariations may result from a combination of depositional bias and signal artefacts. Periods of slow growth and fast growth can be related to respective contraction and dilation of the Y record. One might assume that condensing layers and then analyzing with a relatively large and homogenizing laser spot size may lead to an excessive Y ICP-MS signal. However, it can be shown that averaging across several layers of variable thickness but with constant amplitude merely results in a lower-amplitude measured signal with an otherwise constant average (Fig. S7). However, if climatic shifts impart a seasonal depositional bias, wherein wintertime deposition is limited and growth primarily occurs in the autumn months, then a large-scale shift to high Y and low Sr could be expected (Fig. S8).

6. Conclusions

The interpretation of trace element signatures in speleothems is at times complex due to the multiple factors potentially controlling each, but the examination of multiple proxies, in addition to high-resolution imaging, may help elucidate these factors and improve our understanding of trace element variations. Here, we focus on Sr and Y and derive novel interpretations based on their covariations. Because stalagmite chemistry is strongly influenced by local biogeochemistry and karst processes, these conclusions may be more specific to La Vallina cave but are nevertheless worth exploring in other cave systems. The conceptual model for Sr-Y incorporation is summarized in Fig. 13, and is explained in detail below:

1. Yttrium associates strongly with fluorescent (organic-rich) layers in stalagmites, consistent with the prevailing paradigm that Y and other insoluble cations (e.g. Cu, Zn, Pb) are transported by colloids. The close association suggests that Y is incorporated together with its colloidal host into the calcite lattice, or otherwise separately (after dissociation from its colloid host), but closely spaced in time.
2. D_{Sr} is positively correlated with growth rate, which is ultimately controlled by drip water saturation. This in turn is influenced by cave pCO_2, with maximum saturation coinciding with minimum pCO_2 during winter ventilation. Therefore, Sr peaks likely occur in the winter. The D_{Sr}-growth rate relationship can be demonstrated with two independent methods of growth rate estimation (layer counting and chemical oscillations), However, due to the variable relationship between saturation state and growth rate, some data scatter in the D_{Sr}-growth rate relationship is expected.

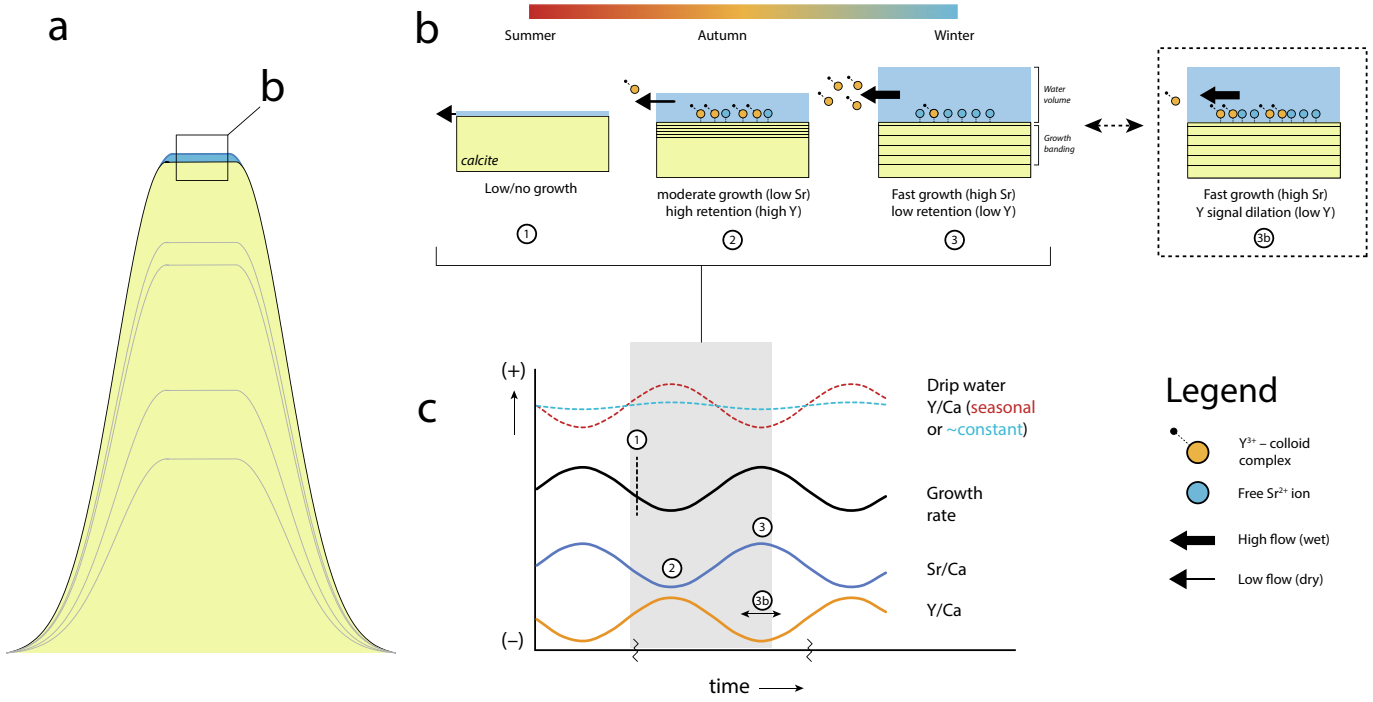

Fig. 13. Graphical representation of the proposed Sr-Y incorporation conceptual model: (a) active stalagmite growth surface, with inset depicting various deposition regimes shown in (b); (b) illustration of summer, autumn and winter flow regimes. (1) Low/zero drip rate in summer precludes deposition; (2) low-moderate drip rate in autumn allows maximum surface retention time for Y-colloid complexes; (3) fast drip rate in winter maximizes Sr partitioning (together with cave ventilation) while minimizing surface retention time for Y-colloid complexes; alternatively, (3b), fast growth dilates the Y concentration making it appear lower. (c) Resultant Sr/Ca and Y/Ca ratios together with growth rate and drip water Y delivery. Note that Sr correlates with growth rate, and that drip water Y delivery may be seasonal, amplifying the effects of increased retention efficiency.

3. Yttrium incorporation is likely heavily influenced by its association with colloidal organic matter, and is likely controlled by a combination of drip water Y flux, retention time on the stalagmite surface, and dilation (stretching/shrinking) during fast or slow growth.
4. Strong seasonal Y peaks may result from optimal deposition conditions in the autumn, which compared to the drier summertime is not moisture-limiting, and compared to wintertime is not excessively wet (i.e., autumnal conditions maximize surface retention time).
5. Inter-annual Sr-Y anti-correlation is most likely generated by a combination of Y dilation and Sr growth rate effects. Fast-growing sections contain low Y, and slow-growing, condensed layers typically show higher Y. A variant on this explanation is ICP-MS signal truncation, whereby increased seasonality biases growth to autumn months, increasing the apparent Y and decreasing apparent Sr (i.e., if deposition only occurs when Y is high, the average Y concentration will likewise be elevated; see Fig. S8).
6. Many active stalagmites show poor Sr-Y anti-correlations and complex fluorescence patterns including evidence for sub-annual banding. Their shared characteristic of summertime dripping raises the possibility that other stalagmites with poor Sr-Y correlation (e.g. fossil stalagmites) have experienced periods of non-seasonal dripping.

Declaration of Competing Interest

The authors declare that they have no known competing financial interests or personal relationships that could have appeared to influence the work reported in this paper.

Appendix A. Supplementary material

Supplementary material to this article can be found online at https://doi.org/10.1016/j.gca.2022.12.023.

References

Baker, A., Genty, D., 1999. Fluorescence wavelength and intensity variations of cave waters. J. Hydrol. 217, 19–34.
Baker, A.J., Mattey, D.P., Baldini, J.U., 2014. Reconstructing modern stalagmite growth from cave monitoring, local meteorology, and experimental measurements of dripwater films. Earth Planet. Sci. Lett. 392, 239–249.
Baker, A., Mockler, N.J., Barnes, W.L., 1999. Fluorescence intensity variations of speleothem-forming groundwaters: Implications for paleoclimate reconstruction. J. Water Resour. Res. 35, 407–413.
Baldini, J.U., McDermott, F., Baldini, L.M., Ottley, C.J., Linge, K.L., Clipson, N., Jarvis, K. E., 2012. Identifying short-term and seasonal trends in cave drip water trace element concentrations based on a daily-scale automatically collected drip water dataset. Chem. Geol. 330, 1–16.
Baldini, J.U., Lechleitner, F.A., Breitenbach, S.F., van Hunen, J., Baldini, L.M., Wynn, P. M., Jamieson, R.A., Ridley, H.E., Baker, A.J., Walczak, I.W., 2021. Detecting and quantifying palaeoseasonality in stalagmites using geochemical and modelling approaches. Quat. Sci. Rev. 254, 106784.
Belli, R., Borsato, A., Frisia, S., Drysdale, R., Maas, R., Greig, A., 2017. Investigating the hydrological significance of stalagmite geochemistry (Mg, Sr) using Sr isotope and particulate element records across the Late Glacial-to-Holocene transition. Geochim. Cosmochim. Acta 199, 247–263.
Bernasconi, S.M., Müller, I.A., Bergmann, K.D., Breitenbach, S.F., Fernandez, A., Hodell, D.A., Jaggi, M., Meckler, A.N., Millan, I., Ziegler, M., 2018. Reducing uncertainties in carbonate clumped isotope analysis through consistent carbonate-based standardization. Geoc. Geophys. Geosys. 19, 2895–2914.
Boch, R., Spoetl, C., Frisia, S., 2011. Origin and palaeoenvironmental significance of lamination in stalagmites from Katerloch Cave, Austria. J. Sed. 58, 508–531.
Borsato, A., Frisia, S., Fairchild, I.J., Somogyi, A., Susini, J., 2007. Trace element distribution in annual stalagmite laminae mapped by micrometer-resolution X-ray fluorescence: implications for incorporation of environmentally significant species. Geochim. Cosmochim. Acta 71, 1494–1512.
Breitenbach, S.F., Bernasconi, S.M., 2011. Carbon and oxygen isotope analysis of small carbonate samples (20 to 100 µg) with a GasBench II preparation device. Rapid Commun. Mass Spectrom. 25, 1910–1914.

Briones, M., Ineson, P., 1996. Decomposition of eucalyptus leaves in litter mixtures. Soil Biol. Bioc. 28, 1381–1388.
Chalmin, E., Perrette, Y., Fanget, B., Susini, J., 2013. Investigation of organic matter entrapped in synthetic carbonates-a multimethod approach. Microsc. Microanal. 19, 132–144.
Cho, K.R., Kim, Y.-Y., Yang, P., Cai, W., Pan, H., Kulak, A.N., Lau, J.L., Kulshreshtha, P., Armes, S.P., Meldrum, F.C., 2016. Direct observation of mineral–organic composite formation reveals occlusion mechanism. Nat. Com. 7, 1–7.
Day, C.C., Henderson, G.M., 2013. Controls on trace-element partitioning in cave-analogue calcite. Geochim. Cosmochim. Acta 120, 612–627.
Demény, A., Németh, P., Czuppon, G., Leél-Őssy, S., Szabó, M., Judik, K., Németh, T., Stieber, J., 2016. Formation of amorphous calcium carbonate in caves and its implications for speleothem research. Sci. Rep. 6, 39602.
DePaolo, D.J., 2011. Surface kinetic model for isotopic and trace element fractionation during precipitation of calcite from aqueous solutions. Geochim. Cosmochim. Acta 75, 1039–1056.
Dos Santos, P., Matias, H., Deus, E., Águas, A., Silva, J.S., 2015. Fire effects on capsules and encapsulated seeds from Eucalyptus globulus in Portugal. Plant Ecol. 216, 1611–1621.
Dreybrodt, W., 1999. Chemical kinetics, speleothem growth and climate. Boreas 28, 347–356.
Esteban-Parra, M., Rodrigo, F., Castro-Diez, Y., 1998. Spatial and temporal patterns of precipitation in Spain for the period 1880–1992. Int. J. Clim. 18, 1557–1574.
Fairchild, I.J., Treble, P.C., 2009. Trace elements in speleothems as recorders of environmental change. Quat. Sci. Rev. 28, 449–468.
Fairchild, I.J., Spötl, C., Frisia, S., Borsato, A., Susini, J., Wynn, P.M., Cauzid, J., 2010. Petrology and geochemistry of annually laminated stalagmites from an Alpine cave (Obir, Austria): seasonal cave physiology. Geol. Soc. Lond. 336, 295–321.
Ferrere, P., Lopez, G., Boca, R., Galetti, M., Esparrach, C., Pathauer, P., 2005. Initial density effect on Eucalyptus globulus growth in a Nelder modified trial. For. Syst. 14, 174–184.
Frisia, S., Borsato, A., Preto, N., McDermott, F., 2003. Late Holocene annual growth in three Alpine stalagmites records the influence of solar activity and the North Atlantic Oscillation on winter climate. Earth Planet. Sci. Lett. 216, 411–424.
Frisia, S., Borsato, A., Drysdale, R., Paul, B., Greig, A., Cotte, M., 2012. A re-evaluation of the palaeoclimatic significance of phosphorus variability in speleothems revealed by high-resolution synchrotron micro XRF mapping. Clim. Past 8, 2039–2051.
Frumkin, A., Stein, M., 2004. The Sahara-East Mediterranean dust and climate connection revealed by strontium and uranium isotopes in a Jerusalem speleothem. Earth Planet. Sci. Lett. 217, 451–464.
Gasparrinia, M., Bakker, R.J., Bechstddt, T., Boni, M., 2003. Hot dolomites in a Variscan foreland belt: hydrothermal flow in the Cantabrian Zone (NW Spain). J. Geoc. Expl. 78, 501–507.
Genty, D., Deflandre, G., 1998. Drip flow variations under a stalactite of the Pere Noel cave (Belgium). Evidence of seasonal variations and air pressure constraints. J. Hydrol. 211, 208–232.
Genty, D., Massault, M., 1999. Carbon transfer dynamics from bomb-^{14}C and $\delta^{13}C$ time series of a laminated stalagmite from SW France-modelling and comparison with other stalagmite records. Geochim. Cosmochim. Acta 63, 1537–1548.
Goede, A., McCulloch, M., McDermott, F., Hawkesworth, C., 1998. Aeolian contribution to strontium and strontium isotope variations in a Tasmanian speleothem. Chem. Geol. 149, 37–50.
Gonzalez-Lemos, S., Müller, W., Pisonero, J., Cheng, H., Edwards, R.L., Stoll, H.M., 2015. Holocene flood frequency reconstruction from speleothems in northern Spain. Quat. Sci. Rev. 127, 129–140.
Green, D.C., Ihli, J., Thornton, P.D., Holden, M.A., Marzec, B., Kim, Y.-Y., Kulak, A.N., Levenstein, M.A., Tang, C., Lynch, C., 2016. 3D visualization of additive occlusion and tunable full-spectrum fluorescence in calcite. Nat. Com. 7, 1–13.
Grinsted, A., Moore, J.C., Jevrejeva, S., 2004. Application of the cross wavelet transform and wavelet coherence to geophysical time series. Nonlinear Processes Geophys. 11, 561–566.
Hartland, A., Fairchild, I.J., Lead, J.R., Borsato, A., Baker, A., Frisia, S., Baalousha, M., 2012. From soil to cave: Transport of trace metals by natural organic matter in karst dripwaters. Chem. Geol. 304, 68–82.
Hartland, A., Fairchild, I.J., Müller, W., Dominguez-Villar, D., 2014. Preservation of NOM-metal complexes in a modern hyperalkaline stalagmite: Implications for speleothem trace element geochemistry. Geochim. Cosmochim. Acta 128, 29–43.
Hartland, A., Zitoun, R., 2018. Transition metal availability to speleothems controlled by organic binding ligands. Geoc. Persp. Let. 2018, 22–25.
Hua, Q., Cook, D., Fohlmeister, J., Penny, D., Bishop, P., Buckman, S., 2017. Radiocarbon dating of a speleothem record of paleoclimate for Angkor, Cambodia. Radiocarb 59, 1873–1890.
Huang, Y., Fairchild, I.J., 2001. Partitioning of Sr^{2+} and Mg^{2+} into calcite under karst-analogue experimental conditions. Geochim. Cosmochim. Acta 65, 47–62.
Jochum, K.P., Scholz, D., Stoll, B., Weis, U., Wilson, S.A., Yang, Q., Schwalb, A., Börner, N., Jacob, D.E., Andreae, M.O., 2012. Accurate trace element analysis of speleothems and biogenic calcium carbonates by LA-ICP-MS. Chem. Geol. 318, 31–44.
Kim, Y.-Y., Ganesan, K., Yang, P., Kulak, A.N., Borukhin, S., Pechook, S., Ribeiro, L., Kröger, R., Eichhorn, S.J., Armes, S.P., 2011. An artificial biomineral formed by incorporation of copolymer micelles in calcite crystals. Nat. Mat. 10, 890–896.
Kim, Y.-Y., Darkins, R., Broad, A., Kulak, A.N., Holden, M.A., Nahi, O., Armes, S.P., Tang, C.C., Thompson, R.F., Marin, F., 2019. Hydroxyl-rich macromolecules enable the bio-inspired synthesis of single crystal nanocomposites. Nat. Com. 10, 1–15.
Kost, O., González-Lemos, S., Rodriguez-Rodriguez, L., Sliwinski, J., Endres, L., Haghipour, N., Stoll, H., 2022. Relationship of seasonal variations in drip water $\delta^{13}C_{DIC}$, $\delta^{18}O$ and trace elements with surface and physical cave conditions of La Vallina Cave, NW Spain. Hydrol. Earth Syst. Sci. Discuss. 2022, 1–42.
Lindeman, I., Hansen, M., Scholz, D., Breitenbach, S., Hartland, A., 2021. Effects of organic matter complexation on partitioning of transition metals into calcite: Cave-analogue crystal growth experiments. Geochim. Cosmochim. Acta 317, 118–137.
Lorens, R.B., 1981. Sr, Cd, Mn and Co distribution coefficients in calcite as a function of calcite precipitation rate. Geochim. Cosmochim. Acta 45, 553–561.
Markowska, M., Fohlmeister, J., Treble, P.C., Baker, A., Andersen, M.S., Hua, Q., 2019. Modelling the ^{14}C bomb-pulse in young speleothems using a soil carbon continuum model. Geochim. Cosmochim. Acta 261, 342–367.
Marzec, B., Green, D.C., Holden, M.A., Coté, A.S., Ihli, J., Khalid, S., Kulak, A., Walker, D., Tang, C., Duffy, D.M., 2018. Amino acid assisted incorporation of dye molecules within calcite crystals. Angew. Chem. Int. Ed. 57, 8623–8628.
Menéndez, M., Álvarez-Alonso, D., de Andrés-Herrero, M., Carral, P., García-Sánchez, E., Pardo, J.F.J., Quesada, J.M., Rojo, J., 2018. The Middle to Upper Paleolithic transition in La Güelga cave (Asturias, Northern Spain). Quat. Int. 474, 71–84.
Meyer, K.W., Feng, W., Breecker, D.O., Banner, J.L., Guilfoyle, A., 2014. Interpretation of speleothem calcite $\delta^{13}C$ variations: Evidence from monitoring soil CO_2, drip water, and modern speleothem calcite in central Texas. Geochim. Cosmochim. Acta 142, 281–298.
Orland, I.J., Bar-Matthews, M., Kita, N.T., Ayalon, A., Matthews, A., Valley, J.W., 2009. Climate deterioration in the Eastern Mediterranean as revealed by ion microprobe analysis of a speleothem that grew from 2.2 to 0.9 ka in Soreq Cave. Israel. Quat. Res. 71, 27–35.
Orland, I.J., Bar-Matthews, M., Ayalon, A., Matthews, A., Kozdon, R., Ushikubo, T., Valley, J.W., 2012. Seasonal resolution of Eastern Mediterranean climate change since 34 ka from a Soreq Cave speleothem. Geochim. Cosmochim. Acta 89, 240–255.
Orland, I.J., Burstyn, Y., Bar-Matthews, M., Kozdon, R., Ayalon, A., Matthews, A., Valley, J.W., 2014. Seasonal climate signals (1990–2008) in a modern Soreq Cave stalagmite as revealed by high-resolution geochemical analysis. Chem. Geol. 363, 322–333.
Paquette, J., Reeder, R.J., 1995. Relationship between surface structure, growth mechanism, and trace element incorporation in calcite. Geochim. Cosmochim. Acta 59, 735–749.
Paton, C., Woodhead, J.D., Hellstrom, J.C., Hergt, J.M., Greig, A., Maas, R., 2010. Improved laser ablation U-Pb zircon geochronology through robust downhole fractionation correction. Geochem. Geophys. Geosyst. 11 (3).
Pearson, A.R., Hartland, A., Frisia, S., Fox, B.R., 2020. Formation of calcite in the presence of dissolved organic matter: Partitioning, fabrics and fluorescence. Chem. Geol. 539, 119492.
Perrette, Y., Delannoy, J.-J., Desmet, M., Lignier, V., Destombes, J.-L., 2005. Speleothem organic matter content imaging. The use of a Fluorescence Index to characterise the maximum emission wavelength. Chem. Geol. 214, 193–208.
Qu, C., Liu, G., Zhao, Y., 2009. Experimental study on the fractionation of yttrium from holmium during the coprecipitation with calcium carbonates in seawater solutions. Geoc. J. 43, 403–414.
Rasband, W., 2012. ImageJ: Image processing and analysis in Java. Astrophys. Source Code Lib., ascl: 1206.1013.
Reimer, P.J., Brown, T.A., Reimer, R.W., 2004. Discussion: reporting and calibration of post-bomb 14C data. Radiocarbon 46, 1299–1304.
Sawada, K., Tan, K., Satoh, K., 2005. Adsorption of lanthanoid ions on calcite. Dalt. Trans., 3291–3296
Shopov, Y., 2009. Activators of luminescence in speleothems as source of major mistakes in interpretation of luminescent paleoclimatic records. Int. J. Speleol. 33 (1/4).
Sliwinski, J., Stoll, H.M., 2021. Combined fluorescence imaging and LA-ICP-MS trace element mapping of stalagmites: Microfabric identification and interpretation. Chem. Geol. 581, 120397.
Stoll, H.M., Cacho, I., Gasson, E., Sliwinski, J., Kost, O., Moreno, A., Iglesias, M., Torner, J., Perez-Mejias, C., Haghipour, N., 2022a. Rapid northern hemisphere ice sheet melting during the penultimate deglaciation. Nat. Com. 13, 1–16.
Stoll, H.M., Day, C., Lechleitner, F., Kost, O., Endres, L., Sliwinski, J., Pérez-Mejías, C., Cheng, H., Scholz, D., 2022b. Distinguishing the vegetation and soil component of $\delta^{13}C$ variation in speleothem records from degassing and prior calcite precipitation effects. Clim. Past Discuss. 2022, 1–30.
Stoll, H., Mendez-Vicente, A., Gonzalez-Lemos, S., Moreno, A., Cacho, I., Cheng, H., Edwards, R.L., 2015. Interpretation of orbital scale variability in mid-latitude speleothem $\delta^{18}O$: Significance of growth rate controlled kinetic fractionation effects. Quat. Sci. Rev. 127, 215–228.
Stoll, H.M., Müller, W., Prieto, M., 2012. I-STAL, a model for interpretation of Mg/Ca, Sr/Ca and Ba/Ca variations in speleothems and its forward and inverse application on seasonal to millennial scales. Geoc. Geophys. Geosys. 13 (9).
Stoll, H.M., Moreno, A., Mendez-Vicente, A., Gonzalez-Lemos, S., Jimenez-Sanchez, M., Dominguez-Cuesta, M.J., Edwards, R.L., Cheng, H., Wang, X., 2013. Paleoclimate and growth rates of speleothems in the northwestern Iberian Peninsula over the last two glacial cycles. Quat. Res. 80, 284–290.

Synal, H.-A., Stocker, M., Suter, M., 2007. MICADAS: a new compact radiocarbon AMS system. Nuc. Inst. Meth. 259, 7–13.
Teng, H.H., Dove, P.M., De Yoreo, J.J., 2000. Kinetics of calcite growth: surface processes and relationships to macroscopic rate laws. Geoc. Geophys. Geosys. 64, 2255–2266.
Terakado, Y., Masuda, A., 1988. The coprecipitation of rare-earth elements with calcite and aragonite. Chem. Geol. 69, 103–110.
Tesoriero, A.J., Pankow, J.F., 1996. Solid solution partitioning of Sr^{2+}, Ba^{2+}, and Cd^{2+} to calcite. Geochim. Cosmochim. Acta 60, 1053–1063.
Thornthwaite, C.W., 1948. An approach toward a rational classification of climate. J. Geograph. Rev. 38, 55–94.
Treble, P.C., Fairchild, I.J., Griffiths, A., Baker, A., Meredith, K.T., Wood, A., McGuire, E., 2015. Impacts of cave air ventilation and in-cave prior calcite precipitation on Golgotha Cave dripwater chemistry, southwest Australia. Quat. Sci. Rev. 127, 61–72.
Tremaine, D.M., Froelich, P.N., 2013. Speleothem trace element signatures: A hydrologic geochemical study of modern cave dripwaters and farmed calcite. Geochim. Cosmochim. Acta 121, 522–545.
Tremaine, D.M., Sinclair, D.J., Stoll, H.M., Lagerström, M., Carvajal, C.P., Sherrell, R.M., 2016. A two-year automated dripwater chemistry study in a remote cave in the tropical south Pacific: Using [Cl^-] as a conservative tracer for seasalt contribution of major cations. Geochim. Cosmochim. Acta 184, 289–310.
Voigt, M., Mavromatis, V., Oelkers, E.H., 2017. The experimental determination of REE partition coefficients in the water-calcite system. Chem. Geol. 462, 30–43.
Wassenburg, J.A., Riechelmann, S., Schröder-Ritzrau, A., Riechelmann, D.F., Richter, D.K., Immenhauser, A., Terente, M., Constantin, S., Hachenberg, A., Hansen, M., 2020. Calcite Mg and Sr partition coefficients in cave environments: Implications for interpreting prior calcite precipitation in speleothems. Geochim. Cosmochim. Acta 269, 581–596.
Wasylenki, L.E., Dove, P.M., De Yoreo, J.J., 2005. Effects of temperature and transport conditions on calcite growth in the presence of Mg^{2+}: Implications for paleothermometry. Geochim. Cosmochim. Acta 69, 4227–4236.
Zhou, H., Wang, Q., Zhao, J., Zheng, L., Guan, H., Feng, Y., Greig, A., 2008. Rare earth elements and yttrium in a stalagmite from Central China and potential paleoclimatic implications. Palaeogeogr. Palaeoclimatol. Palaeoecol. 270, 128–138.